

https://dspace.org/

A photoelastic investigation into the stress concentration factors around rectangular holes in composite plates

Eichenberger, Edward Peter

1993

http://hdl.handle.net/10539/22713

Eichenberger, Edward Peter (1993) A photoelastic investigation into the stress concentration factors around rectangular holes in composite plates, University of the Witwatersrand, Johannesburg, <http://hdl.handle.net/10539/22713>

Downloaded from a DSpace repository. https://dspace.org/

A photoelastic investigation into the stress concentration factors around rectangular holes in composite plates

Edward Peter Eichenberger

A dissertation submitted to the Faculty of Engineering, University of the Witwatersrand, Johannesburg, in fulfilment of the requirements for the degree of Master of Science in Engineering.

Johannesburg, 1993.

Declaration

I declare that this dissertation is my own, unaided work. It is being submitted for the Degree of Master of Science in Engineering in the University of the Witwatersrand, Johannesburg. It has not been submitted before for any degree or examination in any other University.



(Signature of candidate)

30 day of March 1993

Abstract

The stress concentration factors around rectangular holes in carbon-fibre reinforced epoxy plates, subject to uniaxial tensile loads, were investigated experimentally and theoretically.

To obtain theoretical solutions, two approaches were adopted ; the finite element method and the theory of elasticity using the method of complex variable functions.

Reflective photoelasticity was used as the experimental method.

The determination of the stress concentration factor around a rectangular hole in a glass-fibre reinforced plate was attempted using transmissive photoelasticity, but no meaningful results were obtained.

For the analysis using reflective photoelasticity, orthotropic carbon-fibre plates with lay-ups of 0°, 0°/90° and ±45° were considered. The correlation between the experimentally and theoretically derived stress concentration factors was good except for the 0° plate which was susceptible to localised buckling.

It was concluded that reflective photoelasticity can be employed effectively to solve plane stress problems involving composite materials.

Acknowledgements

The assistance of the following people and organisations is gratefully acknowledged:

- my supervisor, Dr H.D. Chandler for supervising this research
- Mark Stone for his valuable ideas and advice
- Jeff van der Merwe of Lyttleton Engineering for guidance in the field of photoelasticity
- Mr John Cooper and the Mechanical Workshop Laboratory staff, especially Japie for the manufacture and modification of experimental equipment
- friends and colleagues for their helpful comments, discussions and assistance
- my family for their support

Contents

Declaration ii
Abstract iii
Acknowledgements iv
Contents v
List of figures vii
List of tables viii

1 Introduction 1

2 Review 4

3 Photoelasticity 6
3.2 The polariscope 7
3.2.1 The plane polariscope 7
3.2.2 The circular polariscope 8
3.3 The stress-optic law 9
3.4 Reflective photoelasticity 10

4 Transmissive photoelasticity 12
4.1 Photo-orthotropic-elasticity 12
4.1.1 Stress-optic law based on a Mohr's circle relationship ... 13
4.1.2 A comparison between isotropic and orthotropic photoelasticity 18
4.2 Specimens 20
4.2.1 The manufacture of photo-orthotropic model material 20
4.2.2 Calibration 21
4.2.3 Description of plate 22
4.2.4 Defects 22
4.3 Experimental equipment 23
4.4 Experimental procedure 24
4.4.1 Determining mechanical properties 24
4.4.2 Calibration procedure 24
4.4.3 Testing procedure 25
4.5 Problems encountered 25
4.6 Results 26
4.7 Discussion 28

5 Reflective photoelasticity 29
5.1 Photoelastic or birefringent coatings 29
5.1.1 Reinforcing effect 30
5.1.2 Effect of Poisson's ratio mismatch 32
5.1.3 Stress analysis 34
5.1.4 Coating material 34

5.2 Specimens 35
5.2.1 Description 35
5.2.2 Manufacture 35
5.2.3 Preparation 35
5.2.4 Calibration 36
5.2.5 Defects 38
5.3 Experimental equipment 39
5.4 Experimental procedure 40
5.4.1 Manufacturing procedure 40
5.4.2 Determining mechanical properties 40
5.4.3 Calibration procedure 41
5.4.4 Testing procedure 42
5.5 Problems encountered 43
5.6 Results 43

6 Analytical methods 45
6.1 Theory of elasticity 45
6.2 The finite element method 49
6.2.1 The finite element model 53
6.3 Results 54
6.4 Discussion 55

7 Correlation of results 57
7.1 Synopsis 68

8 Conclusions 70

9 Recommendations 71

10 References 72

Appendix A The mapping problem
Appendix B Theory of elasticity

List of figures

Figure 3.1	A stressed photoelastic model in a plane polariscope	7
Figure 3.2	A stressed photoelastic model in a circular polariscope - dark field arrangement.	8
Figure 3.3	A reflection polariscope	10
Figure 4.1	Stress notation	13
Figure 4.2	Mohr circle for birefringence	15
Figure 4.3	Plane-stress system	18
Figure 4.4	Isoclinic parameters in uniaxial stress-fields.	19
Figure 4.5	The isochromatics for the composite plate.	26
Figure 4.6	The isochromatics predicted using finite elements.	27
Figure 5.1	Co-ordinate system on a curved boundary.	30
Figure 5.2	Distortion of displacement field through the thickness of the coating due to Poisson's ratio mismatch.	32
Figure 5.3	Four point bending moment applied to the calibration rod.	37
Figure 5.4	Isochromatics for the 0° plate	44
Figure 5.5	Isochromatics for the ±45° plate	44
Figure 5.6	Isochromatics for the 0°/90° plate	44
Figure 6.1	An infinite anisotropic plate with an opening.	46
Figure 6.2	An eight-node quadratic isoparametric element	49
Figure 6.3	A typical finite element mesh of a plate with a rectangular hole.	53
Figure 7.1	The stress distribution around the 0° plate	57
Figure 7.2	The stress distribution around the 0°/90° plate.	58
Figure 7.3	The stress distribution around the ±45° plate.	59
Figure 7.4	The stress distribution around the 0°/90° plate plotted versus the circumference of the hole	60
Figure 7.5	The stress distribution around the ±45° plate plotted versus the circumference of the hole	61
Figure 7.6	Buckling mode shape of the 0°plate	66
Figure A.1	Co-ordinate system used in the Melentiev process	A.2
Figure B.1	Loading on the plate.	B.2

List of tables

Table 4.1	Material properties of transparent composite plate.	22
Table 5.1	Material properties for the carbon fibre prepreg.	37
Table 5.2	Properties for the photoelastic coatings.	37
Table 5.3	Apparent elastic properties of the composite plates	38
Table 5.4	Reflective photoelasticity results	43
Table 6.1	Theory of elasticity results	54
Table 6.2	Finite element method results	54
Table 7.1	Modified elastic properties of carbon plates.	62
Table 7.2	The results of a modified finite element model	64
Table 7.3	Variations in the stress concentration through the thickness of the plate.	65

1 Introduction

Throughout history, the technological development of a nation depended on the advances made in the field of materials. The link has at times been so fundamental that periods in history have been referred to by the predominant material of the time, for example the Stone Age or Iron Age.

With the dawning of the Iron Age in the seventeenth and eighteenth centuries the metal, cast iron had become plentiful for the first time in history. After 1860, the Iron Age gave way to the Steel Age with the discovery of new processes to extract more carbon from iron. During the industrial revolution of the nineteenth century, the development of machines and power generators was closely interrelated with the production of great quantities of metals, especially iron and steel. There were however serious drawbacks to the use of iron and steel in certain applications. These shortcomings were overcome with the development of alloying in which ferrous alloys were produced, each possessing some special characteristic which qualified it for a particular duty. Engineering possibilities increased dramatically.

The requirement of strength combined with lightness in the selection of structural material for an aircraft cannot be easily met by steel. This lead to the development of aluminium alloys and from 1939 onwards airframe construction has relied to a large extent on these alloys.

Since the early 1960's there has been an increasing demand for materials which are stiffer and stronger, yet lighter. The demands made on materials for even better overall performance are so great and diverse that no one material is able to satisfy them - hence the combination of different materials into an integral composite material. Such composite materials systems result in performance unattainable by the individual components. The term "composite material" is being used increasingly as a generic term to describe fibre reinforced plastic.

Composite materials have several advantages over monolithic materials, for example high strength/weight and high stiffness/weight ratios, high fatigue endurance and low density. They also offer the great advantage of a flexible design in that the material may be tailor made for an optimum design. Composite materials represent a giant step in the constant attempts of material optimization.

Designing for high strength/weight or stiffness/weight ratio is of increasing importance in many fields, and unless the design is improved correspondingly, there will be an

increased possibility of failure. Thus the maximum stress in particular, but also the stress distributions, tend to become vital, and it is no longer sufficient to consider just the nominal stresses. The introduction of a hole on a stressed elastic plate causes a redistribution of the stress field. This effect is the greatest on the boundary of a hole and diminishes with distance until, in regions remote from the hole it is negligible. This effect is called stress concentration.

The behaviour of composite laminates with stress concentrations is of great importance in design because of the resultant strength reduction and life reduction due to damage growth around these stress concentrations.

The design and analysis of composite structures relies heavily on experimental data. A variety of experimental methods are used, most of which are applicable to isotropic materials and are adapted to suit composite materials.

Photoelasticity is an experimental stress analysis technique which employs polarised light passing through a stressed photoelastic material to determine the stress or strain distribution in the material. Photoelasticity provides a full-field picture of the stress distribution in a component, allowing design modifications to be undertaken to achieve a minimum mass, functionally adequate part i.e. an optimum design. Photoelasticity also allows the accurate measurement of the stress magnitudes in components with complex geometry or loading conditions.

Photoelasticity has the advantage over strain gauges in determining the stress distribution around an opening, in that it clearly illustrates the position of maximum stress. Readings can therefore be made in the relevant areas being considered. To obtain the stress distribution around an opening using strain gauges, the entire circumference needs to be strain gauged. This still does not guarantee that the position of a strain gauge will lie on the point of maximum stress. This problem is further compounded in the case of a steep stress gradient where the size and accurate alignment of the strain gauge are of prime importance.

This report deals with an experimental investigation into the stress distribution around a rectangular hole in a fibre reinforced composite plate under uniaxial loading.

The composite plates' properties were restricted to being orthotropic i.e. having material properties different in three mutually perpendicular directions and with three mutually perpendicular planes of material symmetry.

It was planned to investigate the effect of varying the fibre orientation, and hence the degree of orthotropy of the plates, on the stress distribution around the rectangular hole.

The experimental program would involve the assessment of the accuracy and applicability of photo-orthotropic-elasticity and photoelastic coatings to determine the stress distribution around the opening in the plate. The experimental data could then be compared with analytical results. The analysis methods used are the classical theory of plane elasticity and the finite element method.

It was anticipated that the investigation would serve to verify the analytical methods, allowing similar analyses to be used as prediction tools without resorting to an experimental investigation.

The report is structured so that the analytical and experimental investigations and results are presented separately. The results obtained from the different investigations are then compared, and finally conclusions are made.

2 Review

Very little work, if any, has been done on the stress distribution around a rectangular hole in an orthotropic plate under uniaxial tensile loading.

The stress concentration factor used in dealing with plates having holes is defined as

$$K = \frac{\sigma_{max}}{\sigma}$$

where K - stress concentration factor
σ_{max} - maximum stress, at edge of hole
σ - applied stress, distant from hole

The stress concentration factor takes into account two effects

- increased stress due to loss in section
- increased stress due to geometry.

The only available theoretical solution for the entire class of stress concentrations in anisotropic materials is for a circular or elliptical hole in an infinite anisotropic plane. Solutions for any other shaped openings are only approximate due to the high degree of mathematical complexity and mapping difficulties introduced by the anisotropic nature of the material.

The stress distribution around rounded rectangular holes in an infinite isotropic plate has been numerically estimated by Sobey[1,2]. The stress concentration factors for rectangular holes of different shapes under various states of stress have been listed by Peterson[3].

Numerous investigators have investigated the problem of a rectangular opening in an anisotropic plate[4,5,6]. Savin[5] has produced a comprehensive collection of approximate solutions to many problems of stress concentration. Solutions to problems involving the plane theory of elasticity using the methods of complex variable function theory have been provided in relatively simple formulae to calculate the stresses.

Numerical methods such as the finite element method can readily be applied to obtain the stress distribution around a hole of any shape in an anisotropic plate of finite width.

Transmissive photoelastic techniques have been applied to glass-fibre reinforced composite materials. Considerable work was performed in the 1960's and 1970's on

the development of orthotropic [illegible]astic material and the development of stress-optic laws which characterize the relations between the optical and mechanical responses of the material. Valuable contributions were made by Sampson[7], who proposed the concept of a Mohr's circle of birefringence, and by Dally and Prabhakaran[8]. A limitation on the technique of photo-orthotropic-elasticity is the difficulty in procuring the model material. Numerous fabrication methods have been reported[9,10].

Some plane stress elasticity problems were solved with photo-orthotropic material[11,12], but these problems have been more or less of a demonstration nature, designed to show the extent to which orthotropic photoelasticity works. The problems investigated have been the compression of a orthotropic disk examining a variety of loading directions relative to the axes of orthotropicity and the investigation of stresses around a bolted joint in tension.

Owing to the difficulties in fabricating photoelastic models of appropriate anisotropy, birefringent coatings are particularly advantageous for analyzing non-isotropic materials. It is often more convenient to bond a birefringent coating to the surface of the structure to determine the surface strains of the component by photoelastically analyzing the coating. The first application of birefringent coatings to fibre reinforced composites appears to have been by Dally and Alfirevich[13] in the late 1960's. They noted the increased fringe density available when coatings were bonded to glass composites, rather than metal, because of higher strength and compliance of the former material. The effect of a mismatch in Poisson's ratio between the specimen material and coating was also examined and a simple formula derived to calculate the stress on a free boundary. Pipes and Dally[14], used classical lamination theory to show that appreciable shear strains may exist at the free boundaries of a laminate, thereby complicating the direct approach of Dally and Alfirevich. They also showed that sub-surface strains at the edge of a discontinuity can be quite different to those on the surface and this could inhibit analyzing such cases by the coating technique. Several works employed birefringent coatings to study the boundary stresses and strains associated with various shaped discontinuities in loaded reinforced composites[15,16,17].

3 Photoelasticity

The unique properties of high strength, low density and adaptability in design and fabrication make composite materials strong candidates for important structural applications. A complete stress analysis of the structure is essential. The inhomogeneity, anisotropy and inelasticity of many composites make the use of experimental techniques for stress analysis indispensable.

Photoelasticity is an experimental technique for stress and strain analysis that is particularly useful for members having complicated geometry, loading conditions or both. For such cases, analytical methods (strictly mathematical methods) may be cumbersome or impossible and analysis by an experimental approach may be more appropriate. Being an optical method, photoelasticity has the advantage of yielding full-field visual as well as quantitative information.

3.1 Fundamentals of polarised light

Light rays are electromagnetic vibrations similar to radio waves. The vibration associated with light is perpendicular to the direction of propagation. A light source emits a train of waves containing vibrations in all perpendicular planes. However, by the introduction of a polarising filter, only one component of these vibrations will be transmitted and such an organised beam is called polarised light.

Light propagates in a vacuum or in air at a speed, C, of $3x10^8$ m/s. In other transparent bodies, the speed, V, is lower and the ratio C/V is called the index of refraction. In a homogeneous body, the index is constant regardless of the direction of propagation or plane of vibration. However, in crystals the index depends upon the orientation of vibration with respect to its axis.

3.2 The polariscope [18,19]

A polariscope is an instrument that measures the relative retardations or phase differences that occur when polarised light passes through a stressed photoelastic model. For experimental stress-analysis work, two types are employed :

- the plane polariscope
- the circular polariscope

The polariscopes consist of a number of optical elements which will be briefly discussed.

Polarisers :- A plane polariser resolves the light wave into two mutually perpendicular components. The component parallel to the axis of polarisation is transmitted while the component perpendicular to the axis is absorbed.

Quarter-wave plate :- A quarter-wave plate resolves polarised light into two orthogonal components and it transmits these components at different velocities. The axis along which the light emerges at a larger velocity is called the fast axis and the other axis, the slow axis. Since the light components travel through the quarter-wave plate at different velocities, they emerge with an angular retardation of 90° or a phase difference of exactly a quarter of a wavelength.

3.2.1 The plane polariscope

The plane polariscope is the simplest polariscope and consists of two linear polarisers and a light source as illustrated in Figure 3.1.

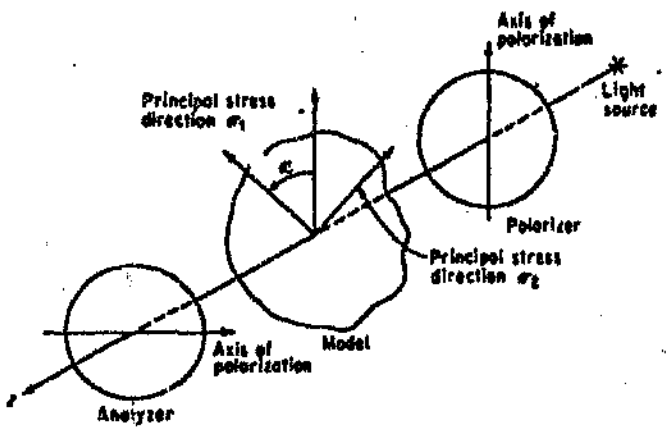


Figure 3.1 A stressed photoelastic model in a plane polariscope [reference 18]

The polariser closest to the light source is called the polariser and the second polariser

is called the analyzer. In the plane polariscope, the two axes of polarisation are crossed.

3.2.2 The circular polariscope

The circular polariscope consists of two polarisers, two quarter-wave plates and a light source. See Figure 3.2.

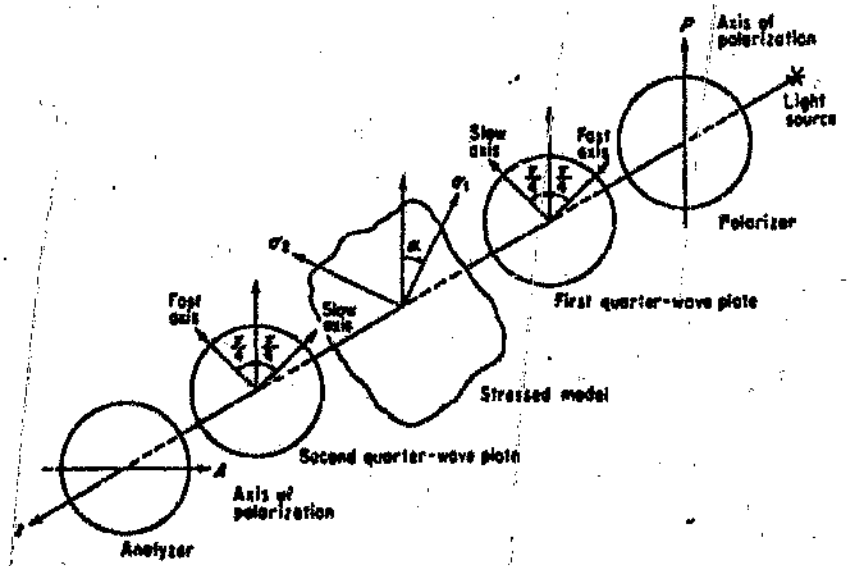


Figure 3.2 A stressed photoelastic model in a circular polariscope - dark field arrangement. [reference 18]

The first optical element after the light source is the polariser, followed by a quarter-wave plate set at 45° to the plane of polarisation. This quarter-wave plate converts the plane polarised light to circularly polarised light. The light is said to be circularly polarised since the quarter-wave plate is at 45° to the polarised light, hence the two components have the same magnitude but are 90° out of phase. Thus if the two components are added vectorially, the tip of the resultant light vector traces out a circle as it rotates.

The second quarter-wave plate converts the circularly polarised light to plane polarised light which passes through the analyzer. If the analyzer and the polariser are crossed, a dark field is produced i.e. the light is extinguished, and if the analyzer and polariser are parallel, a light field is produced.

3.3 The stress-optic law [18,20]

Many transparent, non-crystalline materials that are optically isotropic when free of stress become optically anisotropic when they are stressed. These characteristics persist while loads on the material are maintained but disappear when the loads are removed. This behaviour is known as temporary double refraction and was first observed by Sir David Brewster in 1816. Brewster's Law established that : "The relative change in the index of refraction is proportional to the difference of principal strains". In 1853, Maxwell presented the theory which relates changes in the indices of refraction of a material exhibiting temporary double refraction to the state of stress of the material.

For two dimensional or plane stress problems, the stress-optic law can be written as

$$p - q = \frac{nf}{h} \tag{3.1}$$

where p,q - principal stresses
n - fringe order
f - stress fringe value
h - model thickness

When a stress photoelastic model is in the path of a light ray, the incident light is resolved into components having planes of vibration parallel to the directions of the principal stresses and since these waves traverse the body with different velocities, the waves emerge with a new phase relationship or relative retardation. The two waves are brought together in the polariscope and permitted to come into optical interference.

In a dark-field circular polariscope, extinction of the light occurs if the phase difference, N, is 0,1,2,3,... cycles whilst constructive interference occurs if the phase difference is 1/2, 3/2, 5/2,... cycles. In a light-field circular polariscope, extinction occurs for a phase difference of 1/2, 3/2, 5/2,.. cycles and constructive interference for a phase difference of 0,1,2,3... cycles.

Thus a photoelastic pattern is formed consisting of light and dark bands and is called an isochromatic pattern. The bands are called fringes and the fringe order is defined as the value of N along the band. The number of bands increase in proportion to the applied load and the isochromatic fringe order N at a point is specifically defined as the number of fringes that pass through the point during the application of the external load.

If the stressed model is viewed with the aid of a plane polariscope, extinction of the light occurs when one of the principal-stress directions coincides with the axis of the

polariser. The fringe pattern produced is known as an isoclinic fringe pattern. Elsewhere in the model where the principal stress directions do not coincide with the axes of the polariser, the isochromatic pattern is present. If the polariser and analyzer are maintained in the crossed position and rotated together through 90° whilst the loading remains constant, an isoclinic fringe will pass through every point in the model.

3.4 Reflective photoelasticity [21]

The method of birefringent coatings represents an extension of the procedures of transmissive photoelasticity to the determination of surface strains in opaque bodies. The coating is a thin sheet of birefringent material which is bonded to the body being analyzed. The coating is mirrored at the interface to provide a reflecting surface for the light. When the body is loaded, the displacements on its surface are transmitted to the mirrored side of the coating, where they produce a strain field through the thickness of the coating.

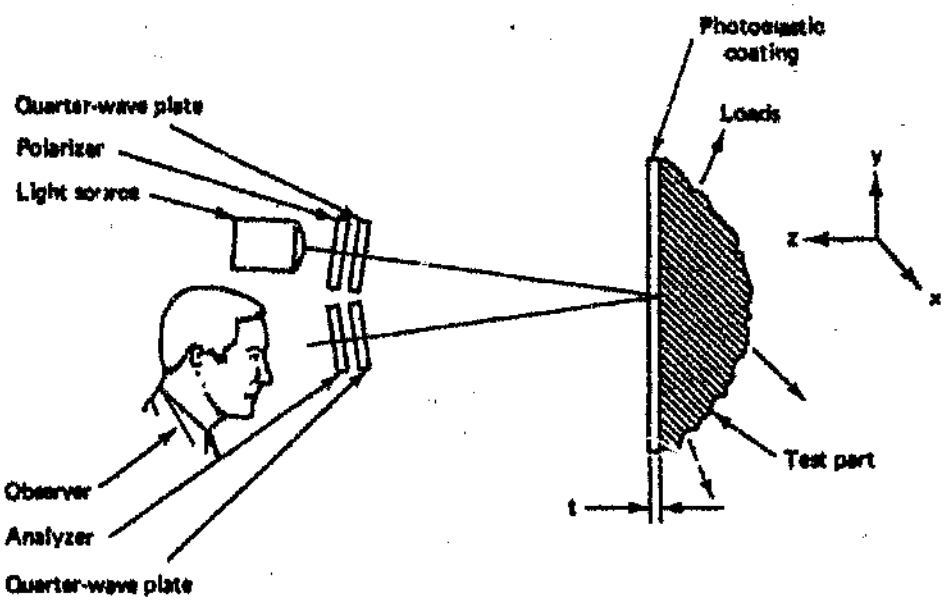


Figure 3.3 A reflection polariscope [reference 21]

The birefringent coating method has advantages over other methods of experimental stress analysis in that it provides full field data and the coating is applied directly to the prototype eliminating the need for a model. The method is also useful in converting complex stress-analysis problems into relatively simple elastic problems in the coating. For example, the anisotropic response of composite materials can be

examined in terms of an isotropic response of the coating.

4 Transmissive photoelasticity

4.1 Photo-orthotropic-elasticity

Significant advances in the development of composite materials have led to an increased use of these materials in high-performance structures. As composite materials are generally orthotropic, suitable methods of experimental stress-analysis had to be developed for structures fabricated from these orthotropic materials.

The use of transmissive photoelasticity applied to a transparent birefringent composite model which has anisotropic elastic and optical properties was initiated by Pih and Knight and Sampson[7] in the late 60's - early 70's. Sampson formulated an orthotropic stress-optic law on the analogy that a circle of birefringence is related to Mohr's circle of stress. Sampson also introduced the concept of three photoelastic constants f_x, f_y and f_{xy} to characterise the photoelastic properties of the orthotropic materials.

Dally and Prabhakaran[8] successfully applied the stress-proportioning concept between the fibres and the matrix to predict the three fundamental photoelastic constants. A stress-optic law was also derived on the basis of stress partitioning between the two constituents in a unidirectionally fibre reinforced laminate and was verified experimentally. However it was stated that "The simplicity of Sampson's theory, coupled with its excellent agreement with experimental result, strongly supports its utilisation over the more complex stress-optic laws developed using stress-strain models." The stress-optic law based on stress proportioning can be considered as a fundamental theoretical proof of Sampson's relation based on analogy only.

Cernosek[22] later concluded that the two seemingly different theories of photoelasticity (Sampson's phenomenological theory and Dally and Prabhakaran's stress proportioning concept) are identical if the heterogeneous nature of the composite is respected.

4.1.1 Stress-optic law based on a Mohr's circle relationship

A stress-optic law was formulated by Sampson[7] based on the concept that the birefringence components contributed by each component of plane stress are combined according to a Mohr circle of birefringence.

The classic derivation of the stress-optic law by Maxwell for physically isotropic materials was based on consideration of the stress-induced changes of refractive index for light polarised in the planes of the two principal stresses. In its most commonly used form, this law is

$$n=\frac{(p-q)h}{f} \tag{4.1}$$

where n = fringe order
p = major principal stress (Pa)
q = minor principal stress (Pa)
h = sheet thickness (m)
f = stress-fringe value (N/m fringe)

or

$$N=\frac{(p-q)}{f} \tag{4.2}$$

where N = observed fringe order per unit thickness (fringe/m)

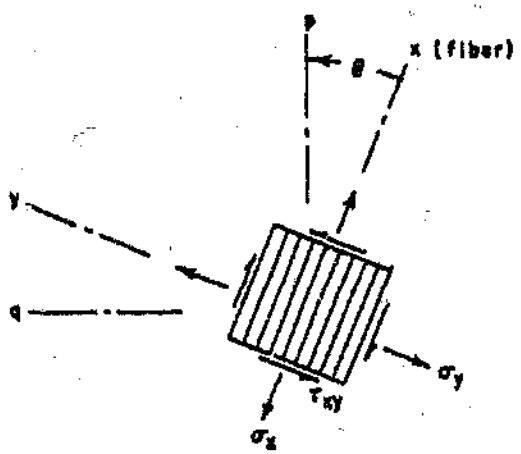


Figure 4.1 Stress notation

The equilibrium of forces on an element in plane stress provides a relationship among the three stress components on the x, y-coordinate system and the two principal stresses. These are

$$\sigma_x = p \cos^2\theta + q \sin^2\theta \tag{4.3}$$

$$\sigma_y = p \sin^2\theta + q \cos^2\theta \tag{4.4}$$

$$\tau_{xy} = \frac{p - q}{2} \sin 2\theta \tag{4.5}$$

where σ = normal stress
τ = shear stress
θ = stress isoclinic parameter
x = fibre longitudinal axis
y = fibre lateral axis

These relationships are the basis of the graphical method for the transformation of co-ordinate systems, i.e., the well-known Mohr circle of stress. Using these relations, the stress-optic law, equation (4.2) can be rewritten in the form

$$N = \sqrt{\left(\frac{\sigma_x}{f} - \frac{\sigma_y}{f}\right)^2 + \left(\frac{2\tau_{xy}}{f}\right)^2} \tag{4.6}$$

Stated in these terms, it is seen that the stress-optic law states that the observed birefringence is composed of two components that are combined vectorially, i.e., a component due to normal stresses on the x and y surfaces of an element and a component due to the shear stress. Furthermore, the two orthogonal components of normal stress each provide a birefringence component that must be combined subtractively with the other before vectorial combination with the shear component of birefringence. These components are defined here as

$$N_x = \frac{\sigma_x}{f}, \quad N_y = \frac{\sigma_y}{f} \quad N_{xy} = \frac{\tau_{xy}}{f} \tag{4.7}$$

In dealing with isotropic materials, it is never necessary to take note of the implication inherent in equation (4.6) i.e. that the observed birefringence is composed of two components that are combined vectorially. For orthotropic materials, on the other hand, equation (4.6) provides an insight essential to the stress-optic law that is postulated here. Consider an element of material in which a unidirectional set of reinforcing fibres is embedded in a matrix. The x and y-directions, Figure 4.1, coincide with the

longitudinal and lateral directions of the fibres, respectively, and the principal stress directions p and q are inclined at an angle θ to the fibre coordinate system. By analogy to the isotropic stress-optic law, equation (4.6), it is postulated that the orthotropic material has three principal stress-fringe values f_x, f_y and f_{xy}, and that the stress system σ_x, σ_y and τ_{xy} produces three components of birefringence

$$N_x = \frac{\sigma_x}{f_x}, \quad N_y = \frac{\sigma_y}{f_y}, \quad N_{xy} = \frac{\tau_{xy}}{f_{xy}} \tag{4.8}$$

By analogy to equation (4.6), the resultant birefringence in plane stress is

$$N = \sqrt{\left(\frac{\sigma_x}{f_x} - \frac{\sigma_y}{f_y}\right)^2 + \left(\frac{2\tau_{xy}}{f_{xy}}\right)^2} \tag{4.9}$$

This, the stress-optic law proposed here for orthotropic materials, also has a graphical representation as a Mohr circle of birefringence.

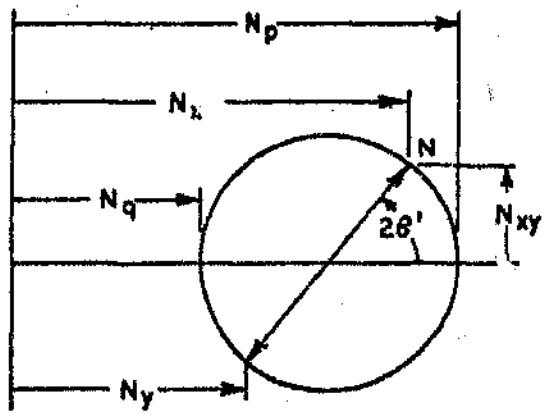


Figure 4.2 Mohr circle for birefringence

It should be noted that the *x*, *y*-coordinate system used here is not the general one, but is instead the fixed reference system coincident with the reinforcing fibre axes. It should also be noted that the components of birefringence have algebraic sign, while the resultant (observed) birefringence *N* does not.

The concept of component birefringences must be considered primarily as a useful abstraction, since experimental measurement of each one individually is not possible in the polariscope.

The proposed two-dimensional Mohr circle for birefringence, Figure 4.2, provides a

visual representation of the relationship among the various birefringence components. The diameter of Mohr's circle of birefringence is equal to the resultant birefringeace N. Relationships analogous to those for stress are evident, e.g.,

$$N^2 = (N_x - N_y)^2 + (2N_{xy})^2 \tag{4.10}$$

$$N_{pq} = \frac{N_x + N_y}{2} \pm \frac{N}{2} \tag{4.11}$$

$$N_x - N_y = N\cos 2\theta' \tag{4.12}$$

and

$$\sin 2\theta' = \frac{2N_{xy}}{N} \tag{4.13}$$

where θ' = optical isoclinic parameter
$N_{x,y,xy}$ = fibre-axis-component birefringence (fringe/m)
$N_{p,q}$ = principal-axis-component birefringence (fringe/m)

The angle θ' between the axis of the major principal component of birefringence N_p and the x-direction obviously does not coincide with angle θ between the p and x-directions of Figure 4.1 unless $f_x = f_y = f_{xy}$, the isotropic case.

From Cernosek[22], for biaxial stress-fields, θ' is related to θ by :

$$\tan 2\theta' = \frac{f_x\left(1 - \frac{q}{p}\right)\sin 2\theta}{f_{xy}\left[\cos^2\theta + \frac{q}{p}\sin^2\theta - \frac{f_x}{f_y}\left(\sin^2\theta + \frac{q}{p}\cos^2\theta\right)\right]} \tag{4.14}$$

and hence for a uniaxial stress field,

$$\tan 2\theta' = \frac{f_x \sin 2\theta}{f_{xy}\left(\cos^2\theta - \frac{f_x}{f_y}\sin^2\theta\right)} \tag{4.15}$$

The isoclinic fringes in orthotropic birefringent models therefore indicate the directions of principal components of birefringence according to a Mohr's circle of birefringence.

Residual birefringence

The differences in the thermoelastic properties of the fibre and resin in the composite may result in residual stresses in the composite during the manufacturing process. These residual stresses result in a residual birefringence.
The cause of residual birefringence is generally due to the shrinkage of the resin which cannot be practically avoided. Hyer and Liu[11] included the residual birefringence into the Mohr circle and represented the resultant birefringence by :

$$N = \sqrt{(N_x - N_y + N_r \cos 2\theta_r)^2 + (2N_{xy} + N_r \sin 2\theta_r)^2} \qquad (4.16)$$

where N_r = residual fringe order per unit thickness
θ_r = orientation of the residual birefringence to the fibre coordinate system

The physical stress-isoclinic parameter θ' observed in the polariscope is

$$\tan 2\theta' = \frac{2N_{xy} + N_r \sin 2\theta_r}{N_x - N_y + N_r \cos 2\theta_r} \qquad (4.17)$$

4.1.2 A comparison between isotropic and orthotropic photoelasticity

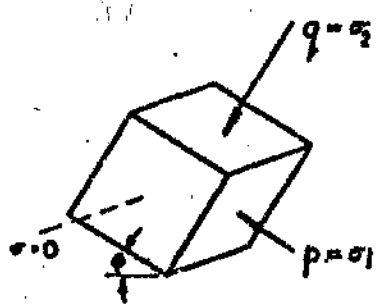


Figure 4.3 Plane-stress system

Consider a small element, oriented such that the faces of the element are principal planes. Let the orientation of the principal planes be defined by the angle φ.

Interpretations of isochromatic patterns

The isochromatic patterns of light and dark bands provide the value of N (the fringe order) throughout the model. The isochromatic fringe order at a point is defined specifically as the number of fringes that pass through the point during the application of the external loads. A change from a dark fringe to an adjacent light fringe represents an increase or decrease of $\frac{1}{2}$ in the value of N.

For an isotropic model, N is directionally proportional to the difference in principal stress.

$$N = \frac{(p - q)}{f} \tag{4.18}$$

For an orthotropic model, the stress-optic law is considerably more complex, however the isochromatic fringes can still be interpreted in terms of principal stresses.

$$N = \frac{p}{f_x}\sqrt{[(\cos^2\theta + \frac{q}{p}\sin^2\theta) - (\sin^2\theta + \frac{q}{p}\cos^2\theta)\frac{f_x}{f_y}]^2 + [\frac{f_x}{f_{xy}}(1 - \frac{q}{p})\sin 2\theta]^2} \tag{4.19}$$

Interpretations of isoclinic patterns

The directions of principal stresses vary continuously from point to point and points at which the principal stresses have a common direction lie along a continuous curve. For any orientation of an isotropic model, the locus of points at which $\varphi=0°$ forms a continuous black curve is called an isoclinic.

Pipes and Dailey[25] concluded that the isoclinics in orthotropic models give neither the composite principal stress directions nor the principal strain direction. According to Mohr's circle of birefringence, the relationship between the optical-isoclinic parameter, θ', and the physical stress-isoclinic parameter, θ, is given for biaxial stress-fields by

$$\tan 2\theta' = \frac{f_x\left(1-\frac{q}{p}\right)\sin 2\theta}{f_m\left[\cos^2\theta + \frac{q}{p}\sin^2\theta - \frac{f_x}{f_y}\left(\sin^2\theta + \frac{q}{p}\cos^2\theta\right)\right]} \qquad (4.20)$$

The isoclinic fringes in an orthotropic birefringence model indicate the direction of the principal components of birefringence according to a Mohr circle of birefringence.

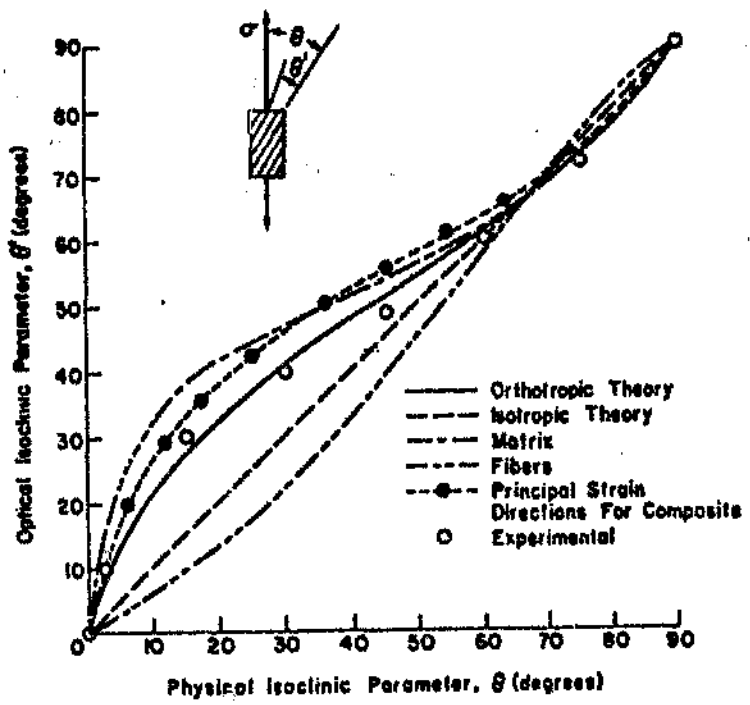


Figure 4.4 Isoclinic parameters in uniaxial stress-fields. [reference 25]

4.2 Specimens

4.2.1 The manufacture of photo-orthotropic model material

The matching of the refractive indices of the reinforcement and the resin in a fibre reinforced photoelastic material, and the elimination of the entrapped air have been recognised as the two most important requirements for transparency.

While a very close matching of the refractive indices is not essential to produce identifiable fringe patterns, a mismatch in the refractive indices causes the reinforcing material to behave as a lens causing a blurring of the higher-order isochromatic fringes thus making the measurement of these fringes difficult.

The reinforcement used was a 450 g/m^2 woven roving supplied by AFI. The roving used is the p366 glass roving. NCS resins provided a high quality casting resin N7036 PA used to make transparent castings. A blend of this resin containing 15 percent methyl methacrylate and cured with two percent methyl ethyl ketone peroxide was determined to have a refractive index which closely matched that of the glass roving[24].

The method of laying up the plates was similar to that suggested by Prabhakaran[10]. The four layers of woven roving were laid-up on a 0.5m x 0.5m glass plate coated with a release agent. The laminate was rolled carefully to remove all the entrapped air. A layer of non-porous plastic film was placed over the wet lay-up to prevent air from re-entering. A second glass plate was lowered on top of the laminate with spacers between the plates to ensure a uniform laminate thickness. The plates were clamped together and the laminate was allowed to cure for 24 hours.

4.2.2 Calibration

The mechanical and optical characteristics of the manufactured plate were required for the finite element analysis.
Specimens were cut along the 0°, 45° and 90° orientations to the major reinforcement directions. The mechanical properties were determined according to BS 2782 : Part 10: Method 1003. The in-plane shear modulus G_{LT} was evaluated using the expression

$$\frac{1}{G_{LT}} = \frac{4}{E_{45°}} - \frac{1-2\nu_{LT}}{E_L} - \frac{1}{E_T} \qquad (4.21)$$

Poisson's ratio was determined by placing strain gauges at 0° and 90° to the fibre orientation which was parallel to the axis of a tensile specimen.

The optical characteristics were determined using bow-tie shaped tensile specimens. A 4 point bending test was unsuccessful due to the out-of-plane deformation of the specimens. The tensile specimens were cut at 0°, 45° and 90° to the major reinforcement direction to measure the stress-fringe values f_L, $f_{45°}$ and f_T respectively. The stress-fringe value f_{LT} could be calculated from[25]

$$\left(\frac{f_{LT}}{f_{45°}}\right)^2 = 1 + \frac{1}{4}\left(\frac{f_{LT}}{f_L}\right)^2\left(1-\frac{f_L}{f_T}\right)^2 \qquad (4.22)$$

Since a woven roving was used, $f_L = f_T$, hence f_{LT} is equal to $f_{45°}$.

The specimens were loaded in tension and the loads recorded for each fringe. Only two fringes were recorded before the fibre de-bonding in the laminate lead to a progressive loss of transparency and eventual failure.

A plot was made of the fringe value vs the load. It was assumed there was no residual birefringence and hence the line passed through the origin. The slope was determined using the method of least squares. The slope of the line divided by the width of the specimen gave the required stress-fringe value in N/metre.fringe. Thus the stress-fringe value is normalised to unit thickness.

Due to the limited material available, only four specimens were tested to obtain each mechanical and optical property. The average of the two values were taken to be representative of the material.

Table 4.1 Material properties of transparent composite plate.

Property	Value	Units
E_L	12.909	GPa
E_T	12.909	GPa
G_{LT}	1.6805	GPa
ν_{LT}	0.218	
f_L	172.3	N/mm.fringe
f_T	172.3	N/mm.fringe
f_{LT}	49.32	N/mm.fringe
Thickness	2.2	mm
Glass mass fraction	45.9	%

4.2.3 Description of plate

A 240mm x 200mm plate with an opening in the centre, was machined from the photo-orthotropic material. The specimen allowed for the position of the clamp, leaving a specimen with a final dimension of 200mm x 200mm. The opening was a square with corner radii of 6.5mm.

4.2.4 Defects

Complete wet-out of the fibres, together with the removal of the entrapped air was not possible. As a result, the plate were not completely transparent with the fibres being visible due to their opaqueness.

Since a considerable amount of monomer was added to the solution, there was a large shrinkage of the resin during the cure. This resulted in a wavy surface finish on one side of the plate.

4.3 Experimental equipment

A 241-22 series polariscope manufactured by Photolastic Inc. was used as the test rig. The collimated light source was removed and replaced by a OSRAM SLG 1000W photographic spotlight mounted behind a ground glass plate which acted as a diffusing screen to create a diffuse white light source.

The polariscope has an eight inch diameter viewing field with the polariser and analyzer mechanically coupled for common rotation during measurement of the isoclinic angle, which is indicated on a dial. The quarter-wave plate could be set in either of two pre-indexed positions within the optical field to create a plane or circular polariscope. The analyzer is independently rotatable to create a light or dark field or to provide for Tardy compensation.

The plate was clamped between two steel jaws mounted in a loading frame. The jaws had knurled grip faces measuring 300mm x 20mm. The loading frame incorporated a screw-operated loading device. An Ametek CA 5000-lbs capacity loadcell was used to record the load. The loadcell was powered with 5V DC using an HBM KWS 906.D amplifier which also displayed the output of the loadcell. The loadcell was calibrated to have a resolution of 23N.

A Pentax single reflex 35mm camera with a 50mm lens was used to obtain a photographic record of the isoclinic and isochromatic fields. A monochromator, a narrow band interferential filter, was used to convert white light into monochromatic light.

To determine the mechanical properties of the composite plate, tensile specimens were tested in a Lloyds MX100K tensile testing machine using a 5kN loadcell. A Roell+Korthaus KG extensometer with a gauge length of 50mm was used to measure the extension of the specimen. The load vs the extension of the specimen was recorded on a Houston Instruments *X-Y plotter*.

To determine Poisson's Ratio, Kyowa KFG-5-120-C1-23 strain gauges were cemented on the specimens using CC-33A adhesive. The strain gauge bridge was powered with 2.5V DC using the HBM KWS 906.D amplifier which also displayed the output voltage. Specimens were clamped in the grips of the Lloyds tensile testing machine and loaded using free weights.

4.4 Experimental procedure

4.4.1 Determining mechanical properties

Elastic modulus :-
Six test specimens were cut for each direction of the material tested i.e. at 0°, 45° and 90° to the fibre-reinforcement orientation. The specimens were machined to the bow-tie shaped Type 1 specimen specified in BS 2782:Part 10:Method 1003. The width and thickness at the midpoint of each specimen was recorded before placing the specimens in the grips of the Lloyds tensile testing machine. The extensometer was attached to the central portion of the specimen. The tests were conducted with the testing speed (rate of separation of the grips) set to 2mm/min. The elongation and corresponding force was recorded on the X-Y plotter. The tests were stopped once an adequate graph of force vs extension was obtained to determine the slope of the line and hence the elastic modulus of the material.

Poisson's ratio :-
Three 200mm × 25mm specimens were machined with their axes parallel to the 0° fibre orientation. The surfaces were lightly sanded with a fine sandpaper and then cleaned with acetone. Two lines were drawn on each specimen, one parallel and one perpendicular to the 0° fibre orientation. A strain gauge was cemented on the specimen parallel to each of the lines. The gauges of two specimens were connected to form two half bridges. A half bridge was formed between the two gauges parallel to the fibre orientation on the two separate specimens, and the other bridge formed between the remaining two gauges perpendicular to the fibre orientation. In this way, each half bridge had one active and one passive gauge for temperature compensation. Whilst one specimen was being tested, the second specimen provided temperature compensation. The specimens were gripped in the Lloyds testing machines' grips. The gauges were excited with 2.5 volts from the amplifier. The output voltage readouts were zeroed. A load was applied using free weights. The output voltages were recorded and Poisson's ratio determined from the ratio of the output voltages of the two half bridges.

4.4.2 Calibration procedure [26]

Four bow-tie shaped tensile specimens were used to calibrate the material : two specimens cut at 0° and two specimens cut at 45° to the major reinforcement direction. The width and the thickness was measured at the midpoint of each specimen before placing the specimens in the clamps of the polariscope's loading frame. A uniaxial load was then applied. The fringe order was observed as the load varied.

4.4.3 Testing procedure [26]

The plate was clamped in the polariscope's loading frame ensuring the plate was not twisted. The polariscope was converted to a plane polariscope and a load of 300N was applied to the plate. The polariser-analyzer assembly was rotated through the angular positions 0° to 90° in steps of 10°. A photograph was taken of the isoclinics at every angular position.

To obtain the stress distribution across the plate, the polariscope was transformed from a plane to a circular polariscope. The load on the plate was increased to 12.7kN. A colour and a monochromatic photographic record of the isochromatics was made.

4.5 Problems encountered

For the optical calibration of the material, tensile specimens were subject to uniaxial load. For tensile specimens, at a given load, the entire specimen should have been in the same state of birefringence since bending effects were judged to be negligible. Yet, during the uniaxial tensile tests, it was not possible to achieve a uniform state of birefringence over the entire specimen. It was slightly lighter or darker toward the one end of the specimen, and it had a distinctive patchy appearance due to the woven rovings. It would appear that the fibres were at a different level of birefringence than the resin. Coupled with this was fibre debonding which occurred in the laminate at higher loads. This lead to a progressive loss of transparency and eventual failure. As a result, only two fringe orders could be identified, and the loads at which they occurred were difficult to determine. Hence, the accurate optical calibration of the material was difficult to achieve.

4.6 Results

Due to the optical insensitivity of the fibre-resin combination coupled with the streaky and patchy appearance of the isochromatic, no clear isochromatic could be observed in order to make accurate stress magnitude predictions.

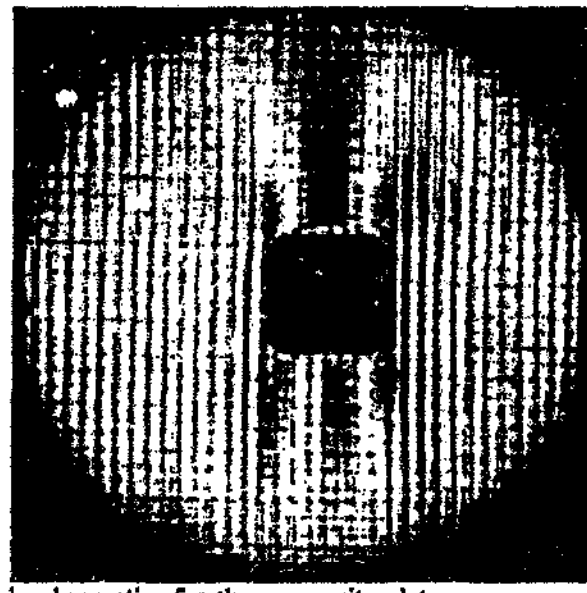


Figure 4.5 The isochromatics for the composite plate.

The finite element analysis of the stressed plate predicted a maximum stress concentration of 3.13. The stresses calculated at each node of the finite element model were used to predict the fringe order, and a contour plot of these values which represent the isochromatics is presented in Figure 4.6.

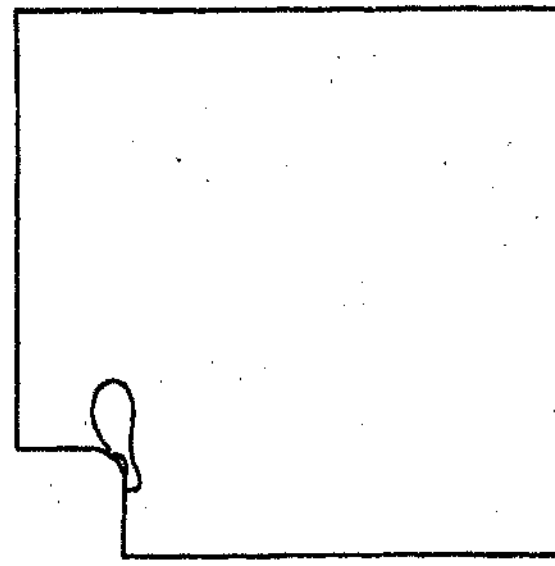


Figure 4.6 The isochromatics predicted using finite elements.

The finite element model predicted the first and second isochromatic fringes. In the experimental results, the zero fringe occurred at the midpoint of the upper and lower end of the rectangle, and the first fringe was visible around the corners of the rectangle. An attempt to obtain fringe multiplication by superimposing a photograph of a light and dark field of the isochromatics was unsuccessful.

4.7 Discussion

The attempt to use photo-orthotropic-elasticity to determine the stress distribution around the rectangular hole was unsuccessful.

Compared to isotropic photoelasticity, photo-orthotropic-elasticity does not seem to be as accurate due to the lack of good fringe resolution. The patchy appearance of the isochromatics could be partly attributed to the woven roving employed in the model material. By eliminating the woven roving, and replacing it with unidirectional fibres, it might be possible to improve the appearance of the isochromatics, but it was felt that the fringe resolution and optical sensitivity of the material would still be inadequate for stress magnitude calculations.

The emphasis on research into photo-orthotropic-elasticity, has been on the development of basic techniques of stress analysis rather than on the application of these techniques. The orthotropic stress laws appear to be valid and model materials need to be improved to allow photo-orthotropic-elasticity to play a useful role in stress analysis of composite structures.

5 Reflective photoelasticity

5.1 Photoelastic or birefringent coatings

The normal behaviour of transmission photoelasticity cannot be applied to most composite materials since suitable anisotropic, transparent birefringent materials are not readily available. It is possible however, to employ birefringent coatings bonded to the surface of anisotropic bodies to analyze the stress field in the material.
The strain field in the loaded anisotropic body produces a photoelastic response in the isotropic birefringent coating which can be interpreted to establish the strains in the specimens. The *stress-strain* relations for anisotropic media are employed to establish the associated stress field. Thus the birefringent coating is essentially employed to convert an anisotropic problem to an isotropic problem. Observation of the coating by means of a reflective polariscope gives a fringe pattern which is related to the surface strains of the specimen.

The strain-optic law for photoelastic coatings is similar to the stress-optic law for transmissive photoelasticity except the path length is now 2h rather than h.

$$\varepsilon_1 - \varepsilon_2 = Nf = N\frac{\lambda}{2hK} \qquad (5.1)$$

where

$\varepsilon_1, \varepsilon_2$	Principal strains
N	Fringe order
f	Fringe value or coating sensitivity (m/m per fringe)
λ	Wavelength of light
h	Thickness of coating
K	Strain-optic coefficient for the coating

5.1.1 Reinforcing effect [27,16,28]

When a part is coated with a layer of plastic and subjected to a load, the plastic coating carries a fraction of the load, and the strain on the part is thereby reduced. The extent of the reinforcement depends on the relative elastic properties and thicknesses of the coating and structure. For plane stress structures, the principal strain difference, $(\varepsilon_1-\varepsilon_2)$, in the uncoated structure relative to that in the coated structure,$(\varepsilon'_1-\varepsilon'_2)$, is given by

$$\varepsilon_1 - \varepsilon_2 = \frac{1}{C_s}(\varepsilon'_1 - \varepsilon'_2) \tag{5.2}$$

$$\frac{1}{C_s} = 1 + \frac{t_c E_c}{t_s E_{s\theta}}\left(\frac{1+\nu_{s\theta}}{1+\nu_c}\right) \tag{5.3}$$

where
- t_c thickness of the coating
- t_s thickness of the specimen
- E_c modulus of elasticity of the coating
- ν_c Poisson's ratio of the coating
- $E_{s\theta}$ modulus of elasticity of the material in the θ direction
- $\nu_{s\theta}$ Poisson's ratio of the material in the ν direction.

If the principal material directions or the major fibre reinforcement directions of an orthotropic laminate are the x and y axes, $\nu_{s\theta}$ and $E_{s\theta}$ are given by :

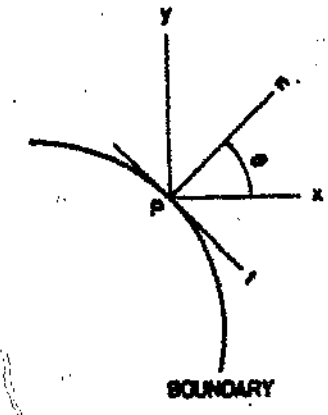


Figure 5.1 Co-ordinate system on a curved boundary.

$$\nu_{xy} = \frac{\frac{\nu_{xy}}{E_y}(\sin^4\theta + \cos^4\theta) + (\frac{1}{G_{xy}} - \frac{1}{E_x} - \frac{1}{E_x})\sin^2\theta\cos^2\theta}{\frac{1}{E_y}\cos^4\theta + \frac{1}{E_x}\sin^4\theta + (\frac{1}{G_{xy}} - \frac{2\nu_{xy}}{E_y})\sin^2\theta\cos^2\theta} \qquad (5.4)$$

$$\frac{1}{E_{xy}} = \frac{1}{E_y}\cos^4\theta + \frac{1}{E_x}\sin^4\theta + (\frac{1}{G_{xy}} - \frac{2\nu_{xy}}{E_y})\sin^2\theta\cos^2\theta \qquad (5.5)$$

where E_x, E_y Modulus of elasticity in the x and y directions

G_{xy} Shear modulus in the x-y plane

ν_{xy}, ν_{yx} Poisson's ratio for transverse strain when stressed in the x and y directions

5.1.2 Effect of Poisson's ratio mismatch [29,13]

The directional dependence of the elastic properties of anisotropic media can produce an appreciable mismatch in Poisson's ratio between the coating and the specimen. Different fibre-matrix combinations, fibre orientations and variations in the laminate stacking sequence can affect the Poisson's ratio of a composite and thereby aggravate the mismatch. By varying the fibre orientation in a composite material, the Poisson's ratio is varied which could result in extremely low values. As a result of this, large mismatches in Poisson's ratio can occur between the coating and the specimen.

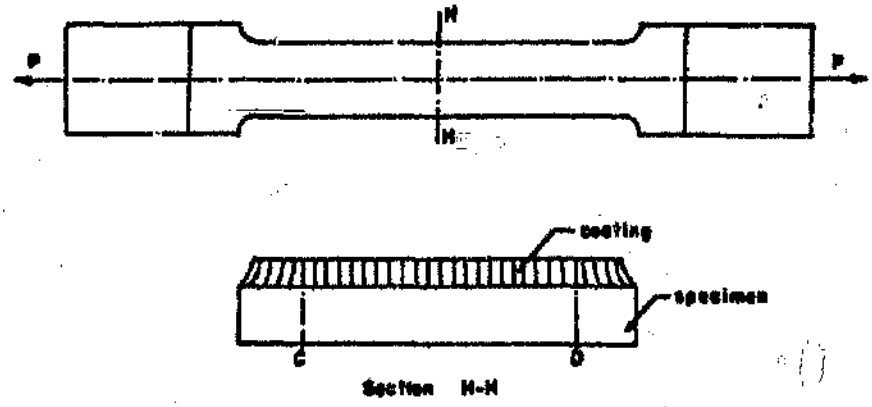


Figure 5.2 Distortion of displacement field through the thickness of the coating due to Poisson's ratio mismatch. [reference 13]

This difference in Poisson's contraction produces a distortion of the displacement field through the thickness of the coating, which is particularly pronounced at the boundaries.

If the coating is bonded, the strains in the structure and the coating will be identical at the interface. However, there will be a tendency for the upper layers of the coating to assume the state of deformation of the equivalent unbonded coating, and a transition between conditions of bonded and unbonded coatings will develop through the coating thickness.

The principal strains tangential to the boundary are assumed to remain constant throughout the coating thickness and equal to ε_1 i.e.

$$\varepsilon_1^c = \varepsilon_1^s \tag{5.6}$$

The distortion of the strain field occurs primarily in the transverse direction due to the difference in Poisson's contraction.

At the interface, the transverse strain in the coating ε_2^c is controlled by the specimen and

$$\varepsilon_2^c = \varepsilon_2^s = -\nu^s \varepsilon_1^s \tag{5.7}$$

because of the bond. However, at the free surface, the transverse strain in the coating is entirely due to the Poisson contraction with

$$\varepsilon_2^c = -\nu^c \varepsilon_1^c = -\nu^c \varepsilon_1^s \tag{5.8}$$

The average value of ε_2^c through the thickness of the coating is bounded by the two values given by equations (5.7) and (5.8). Thus the fringe-order response of the coating is bounded by:

$$\frac{(1+\nu^s)\varepsilon_1^s}{f} < N < \frac{(1+\nu^c)\varepsilon_1^s}{f} \tag{5.9}$$

where f is the coating sensitivity accounting for the thickness of the coating. Since N is bounded, it is convenient to write the equation for N in terms of the strain ε_1 as:

$$N = \left[\frac{1+\nu^s+C_\nu(\nu^c-\nu^s)}{f}\right]\varepsilon_1^s \tag{5.10}$$

where C_ν is a correction factor to be determined for the influence of mismatch at the boundary.

It is clear from equation (5.9) that the magnitude of the distortion is controlled by the mismatch parameter

$$\frac{1+\nu^c}{1+\nu^s} \tag{5.11}$$

Post and Zandman[29] indicated that the fringe order on the boundary is given by

$$N = \left(\frac{1+\nu^c}{f}\right)\varepsilon_1^s \tag{5.12}$$

and the fringe order at interior points in a tension specimen is given by

$$N = \left(\frac{1+\nu^s}{F}\right)\varepsilon_1^s \tag{5.13}$$

5.1.3 Stress analysis [13]

On the free boundaries of a geometric discontinuity, the normal and the shear stresses vanish. The tangential stress is therefore given by

$$\sigma_t = E_t \varepsilon_t \tag{5.14}$$

where E_t is the modulus tangent to the boundary at the point of interest.

From equations (5.10) and (5.12), the tangential stress at the boundary of the discontinuity in an anisotropic material becomes

$$\sigma_t = E_t\left(\frac{f}{1+\nu^2}\right)N \tag{5.15}$$

Since both N and E_t can vary as a function of the position around a discontinuity in an anisotropic material, the maximum tangential stress need not necessarily coincide with the position of the maximum fringe order.

5.1.4 Coating material [30,31]

For birefringent coating analysis, it is desirable that the coating be adequately sensitive, while sufficiently thin and compliant to minimise any reinforcing effect. The sensitivity of the coating is expressed by the fringe value, f. The fringe value represents the difference in principal strains required to produce one fringe. The lower this parameter is, the more sensitive the coating. The value of f can be reduced by increasing the thickness of the coating or employing a more sensitive birefringent coating.

Poisson's ratio should also be as close to that of the structural material as possible.

5.2 Specimens

5.2.1 Description

Three carbon fibre reinforced epoxy plates were manufactured. Each plate measured 240mm x 200mm with a square opening in the centre. The opening was 50mm long with a radius in each corner of 5mm. The plates allowed for the positioning of the testing machine's clamps, leaving a specimen with a final dimension of 200mm x 200mm. Aluminium tabs were bonded along the edges of the plate to be clamped to ensure a good grip.

The specimens were made from 12 layers of Brochier Vicotex NCHR 913/35%/135 HTA supplied by Ciba Geigy. This is an epoxy based preimpregnated laminate with unidirectional carbon fibres. The resin content is claimed to be 35% and the nominal thickness per layer is 0.13mm. The three orthotropic laminates chosen were 0°, 0°/90° and ±45°. The plates had a nominal thickness of 1.6mm.

5.2.2 Manufacture

Three 250mm square plates were laid up with the desired fibre orientations. The plates were then vacuum bagged on a flat aluminium table which was placed in an autoclave. The laminate was cured for 2½ hours at 120°C and 5.5 bar in accordance with the manufacturers recommended cure cycle for the material. Once cured the plates were machined to size and the square opening was cut into the plate. The aluminium tabs were then bonded to the plate using an epoxy adhesive.

5.2.3 Preparation [32]

For the reflective photoelastic analysis, a photoelastic coating needs to be bonded to the surface of the plate. PS-1 sheeting, supplied by Photolastic Inc., was used because of its high sensitivity and a reflective surface was provided on the one surface of the flat sheeting. Two different thicknesses of sheeting were used to obtain the required optical sensitivity. 2mm thick PS-1B was applied to the 0° and 0°/90° carbon plates, whilst a 0.5mm thick PS-1D was applied to the ±45° carbon plate. The sheeting was bonded to the carbon plates using a cold setting, slow curing epoxy adhesive Araldite

AY103 and hardener HY991.

Due to the symmetry of the problem, only one quarter of the plate was covered wit the photoelastic coating. Once the adhesive had cured for 24 hours, the sheeting was trimmed to fit the opening using a fret saw and filed for an accurate finish.

5.2.4 Calibration [33]

The elastic modulus and Poisson's ratio of the photoelastic coating were taken from the literature available.

The mechanical properties of the carbon fibre prepreg were required for the finite element analysis. The mechanical properties were determined according to BS 2782 : Part 10: Method 1003.
Two plates were laid up. The one plate had a unidirectional lay-up and five bow-tie specimens were cut at 0° and another five specimen cut at 90° to the fibre orientation. The second plate had a 0°/90° lay-up and five specimens were cut at 45° to the major fibre reinforcement directions. The in-plane shear modulus G_{LT} was evaluated using the classical lamination theory and the moduli E_1, E_2 and $E_{45°}$.
Poisson's ratio was determined by placing strain gauges at 0° and 90° to the fibre orientation on a specimen in which the fibre orientation was parallel to the axis of the specimen.

In order to translate the measured fringe orders in a photoelastic coating into strains or stresses in the coated plate, it is necessary to determine the fringe value, f, of the coating. The fringe value accounts for the thickness of the coating and the nature of the light source.
To calibrate the coating, a 50mm x 11mm strip of the material was bonded to a 150mm x 11mm x 6.25mm rectangular aluminium rod. This aluminium rod was subjected to a four point bending moment. The fringe order of the coating was recorded for a specified load. The fringe value was calculated, compensating for the bending effects.

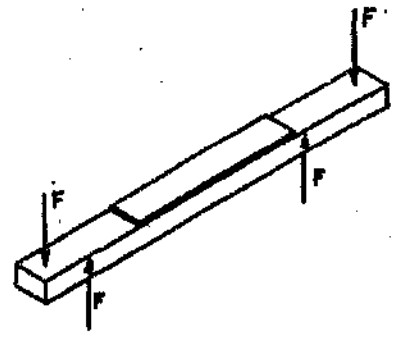


Figure 5.3 Four point bending moment applied to the calibration rod.

Table 5.1 Material properties for the carbon fibre prepreg.

Property	Value	Units
E_L	129.933	GPa
E_T	8.836	GPa
G_{LT}	4.527	GPa
ν_{LT}	0.3	

Table 5.2 Properties for the photoelastic coatings.

Coating	Property	Value	Units
PS-1B	E	2.5	GPa
	ν	0.38	
	f	918	m/m per fringe
	thickness	2	mm
PS-1D	E	2.5	GPa
	ν	0.38	
	f	3781	m/m per fringe
	thickness	0.5	mm

The elastic properties of the composite plates were determined using classical lamination theory and the four elastic constants of the carbon prepreg.

Table 5.3 Apparent elastic properties of the composite plates

Construction	E_{11} (GPa)	E_{22} (GPa)	G_{12} (GPa)	ν_{12}	ν_{21}
[0°]	129.933	8.836	4.527	0.3	0.0204
$[0°/90°]_s$	69.693	69.693	4.527	0.0382	0.0382
$[\pm 45°]_s$	16.097	16.097	33.564	0.7779	0.7779

5.2.5 Defects

The cured carbon prepreg plates had ripples on the side which were not cured up against the aluminium table. This resulted in slight variations in the thickness of the plates.

5.3 Experimental equipment

A model 031 reflection polariscope was used. The instrument consists of two primary components:- an optical head assembly and a high intensity light source. Included in the optical head and integrated by a common frame are two polarizer / quarterwave plate assemblies. By setting the quarterwave plates into either of the two preindexed positions, the principal strain directions or the difference in principal strains at a point in the coating can be measured. The analyzer is independently rotatable to create a light or dark field or to provide for Tardy compensation.

A model 232 uniform-field digital compensator was also employed to allow accurate fringe-order measurement. The compensator was a Babinet-Soleil null-balance compensator.

A model 137 telemicroscope consisting of a microscope barrel with a 6X objective lens and a 10X eyepiece linked to a f/3.5, 43-86mm zoom lens was used. This allowed for close-up examinations of the fringe orders around the stress concentrations in the plate.

A Pentax single reflex 35mm camera with a 50mm lens was used to obtain a photographic record of the isoclinic and isochromatic fields.

To determine the mechanical properties of the composite plate, tensile specimens were tested in a Lloyds MX100K tensile testing machine using a 100kN loadcell. A Roell+Korthaus KG extensometer with a gauge length of 50mm was used to measure the extension of the specimen. The load versus the extension of the specimen was recorded on a Houston Instruments X-Y plotter. The Lloyds tensile testing machine was also used to apply a constant load on the plate whilst the fringe orders were being measured.

To determine Poisson's ratio, Kyowa KFG-5-120-C1-23 strain gauges were cemented on the specimens using CC-33A adhesive. The strain gauge bridge was powered with 2.5V DC using the HBM KWS 906.D amplifier which also displayed the output voltage. Specimens were clamped in the grips of the Lloyds tensile testing machine and loaded using free weights.

5.4 Experimental procedure

5.4.1 Manufacturing procedure

To manufacture a single carbon plate, twelve 250mm square pieces were cut from the roll of uncured carbon fibre prepreg. The layers were laid-up with the correct fibre orientation ensuring the laminate was symmetrical about its middle plane. The laminate was placed on release film on a flat aluminium table. This was done to achieve a smooth surface finish. The laminate was then covered with peel ply, release film, breather cloth and finally a non-porous bag. A vacuum was applied and the aluminium table placed in an autoclave. The laminate was then cured for 2½ hours at 120°C and 5.5 bar. Once cured, the plate was machined to its final dimensions and the hole was machined in the plate. Aluminium tabs were then bonded to the edges of the plate to be clamped.

A 110mm square piece of photoelastic coating was cut and bonded to the one quarter of the smooth side of the plate. Once cured, the coating was cut to the same dimension as the hole.

5.4.2 Determining mechanical properties

Elastic modulus :-
Five test specimens were cut for each direction of the material tested i.e. at 0° and 90° to the fibre-reinforcement orientation and five specimens with a fibre-reinforcement orientation of ±45°. The specimens were machined to the bow-tie shaped Type 1 specimen specified in BS 2782:Part 10:Method 1003. The width and thickness at the midpoint of each specimen was recorded before placing the specimens in the grips of the Lloyds tensile testing machine. The extensometer was attached to the central portion of the specimen. The tests were conducted with the testing speed (rate of separation of the grips) set to 2mm/min. The elongation and corresponding force was recorded on the X-Y plotter. The tests were stopped once an adequate graph of force vs extension was obtained to determine the slope of the line and hence the elastic modulus of the material.

Poisson's ratio :-

Three 200mm × 25mm specimens were machined with their axes parallel to the 0° fibre orientation. The surfaces were lightly sanded with a fine sandpaper and then cleaned with acetone. Two lines were drawn on each specimen, one parallel and one perpendicular to the 0° fibre orientation. A strain gauge was cemented to the specimen parallel to each of the lines. The gauges of two specimens were connected to form two half bridges. A half bridge was formed between the two gauges parallel to the fibre orientation on the two separate specimens, and the other bridge formed between the remaining two gauges perpendicular to the fibre orientation. In this way, each half bridge had one active and one passive gauge for temperature compensation. Whilst one specimen was being tested, the second specimen provided temperature compensation. The specimens were gripped in the Lloyds testing machines' grips. The gauges were excited with 2.5 volts from the amplifier. The output voltage readouts were zeroed. Load was applied using free weights. The output voltages were recorded and Poisson's ratio determined from the ratio of the output voltages of the two half bridges.

5.4.3 Calibration procedure [34]

The fringe value, f, for each of the photoelastic coatings was determined. A thin strip of the coating, 50mm x 11mm, was bonded to a rectangular aluminium rod, 150mm x 11mm x 6.25mm. The exact dimensions of the rod were recorded before it was loaded with a four point bending moment to create a uniform strain throughout the whole coating. The fringe order of the coating was recorded for a specific bending moment. The stress and hence the strain on the surface of the aluminium beam was calculated, and the fringe values were compensated for the bending effects. The fringe value was determined since the strain in the coating together with the observed fringe order was known.

5.4.4 Testing procedure [35,36]

The plate was clamped in the Lloyds tensile testing machine, ensuring the plate was not twisted, and the positions where fringe measurements were to be made were marked on the perimeter of the opening. A tensile load was applied to the plate until approximately two isochromatic fringes were visible around the edge of the hole. At each test point, the polarisation axes of the polariser and analyzer were aligned with the direction of principal strain. The control knob on the compensator was then rotated counterclockwise until a black zero-order fringe crossed the test point. The counter reading on the compensator was recorded and converted to fringe order.
If residual birefringence existed in the coating before the tensile load was applied, the residual stresses were recorded and the final readings adjusted to compensate for them.

5.5 Problems encountered

Holes had been drilled through the aluminium tabs to allow the grips to be bolted closed. The presence of these holes resulted in considerable stresses being measured by the photoelastic coatings.

5.6 Results

The maximum and minimum stress concentrations determined using photoelasticity are listed in table Table 5.4

Table 5.4 Reflective photoelasticity results

Plate	Maximum stress concentration and position			Minimum stress concentration and position		
	Value	x	y	Value	x	y
0°	3.304	20	15	-0.155	0	20
±45°	5.439	18.83	18.21	-1.000	0	20
0°/90	3.025	19.98	15.44	-1.367	2	20

The figures on the following page are a photographic record of the isochromatics for the three plates.



Figure 5.4 Isochromatics for the 0° plate

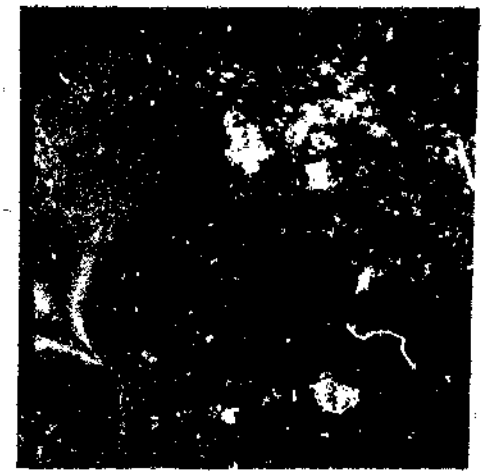


Figure 5.5 Isochromatics for the ±45° plate



Figure 5.6 Isochromatics for the 0°/90° plate

6 Analytical methods

6.1 Theory of elasticity [4,5]

The analysis of the stress distribution in an anisotropic plate with various shaped openings was studied by the Russians Lekhnitskii[4] and Savin[5] in the early 1940's. Green[6] also studied openings in orthotropic plates during the same period. The problem involved the stress distribution in wooden structures - wood, especially plywood, being used in aircraft structures.

An anisotropic, homogenous plate weakened by an opening was considered. When the opening is small in comparison with the plate size and not located at the plate edge, the problem can be simplified by assuming the plate to be infinite and the effect of the external edge can be disregarded.

An exact solution of problems concerning the stress distribution in an anisotropic plate with an opening is known only for an elliptic or circular opening. There are no accurate solutions for any other openings due to the mathematical difficulties involved. For the case where the opening differs from that of an ellipse or circle, it is possible to find an approximate solution for such a plate by introduction of a parameter which will characterise the deviation of the opening from an ellipse or circle.

The contour of such an opening can be represented by the equations:

$$x = a\left[\cos\theta + \varepsilon\sum_{n=1}^{N}(a_n\cos n\theta + b_n\sin n\theta)\right]$$
$$y = a\left[c\sin\theta + \varepsilon\sum_{n=1}^{N}(-a_n\sin n\theta + b_n\cos n\theta)\right] \qquad (6.1)$$

When $\varepsilon=0$, we obtain an ellipse with semi-axes a and ac. In the case of small ε, we obtain a figure which will differ slightly from that of an ellipse.

Forces X_n and Y_n are distributed along the opening edge (per unit area) and their resultant is equal to zero.
The stress distribution of σ_n needs to be determined along the opening edge. The solution of the problem can be obtained by making two transformations:

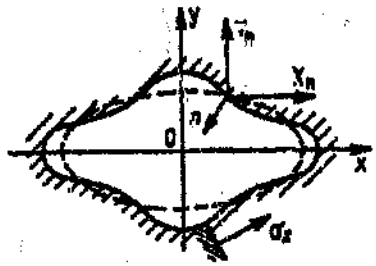


Figure 6.1 An infinite anisotropic plate with an opening. [reference 4]

1 - An infinite plate with an opening is conformally transformed into a finite plate in the shape of the opening.

Assuming the forces X_n and Y_n depend on s, they are expanded into Fourier series according to this parameter to obtain

$$\begin{aligned} \int_0^s Y_n ds + c1 &= \sum_{k=0} \varepsilon^k \left[\overline{\alpha_{k0}} + \sum_{m=1}^{\infty} (\alpha_{km}\sigma^m + \overline{\alpha_{km}}\sigma^{-m}) \right] \\ -\int_0^s X_n ds + c2 &= \sum_{k=0} \varepsilon^k \left[\overline{\beta_{k0}} + \sum_{m=1}^{\infty} (\beta_{km}\sigma^m + \overline{\beta_{km}}\sigma^{-m}) \right] \end{aligned} \tag{6.2}$$

where α_{km}, β_{km} are known coefficients which depend on the force distribution at the opening edge.

2 - An infinite plate with an opening is conformally transformed to an infinite plate in the ζ-plane with an opening in the shape of a unit circle.

The transformation is

$$z = a\left[\frac{1+c}{2}\zeta + \frac{1-c}{2}\frac{1}{\zeta} + \varepsilon\psi(\zeta)\right] \tag{6.3}$$

where

$$\psi(\zeta) = \sum_{n=1}^{N} (a_n + ib_n)\zeta \tag{6.4}$$

The stress function and hence the components of stress can now be expressed in terms of functions of complex variables $\varphi_1(z_1')$ and $\varphi_2(z_2')$ of variables z_1' and z_2'.

The boundary conditions for these functions for given external forces will be

$$2Re[\varphi_1(z_1') + \varphi_2(z_2')] = \int_0^s Y_n ds + c1$$
$$2Re[\mu_1\varphi_1(z_1') + \mu_1\varphi_2(z_2')] = -\int_0^s X_n ds + c2 \tag{6.5}$$

Functions φ_1 and φ_2 are represented in a form of series ordered according to the powers of parameter ε.

$$\varphi_1 = \varphi_{10} + \varepsilon\varphi_{11} + \varepsilon^2\varphi_{12} + \ldots\ldots$$
$$\varphi_2 = \varphi_{20} + \varepsilon\varphi_{21} + \varepsilon^2\varphi_{22} + \ldots\ldots \tag{6.6}$$

Substituting boundary values φ_1 and φ_2 [equation (6.2)] into boundary conditions [equation (6.5)] and comparing coefficients of the same power of ε, a solution is obtained for φ_{1k} and φ_{2k}.

σ_n can now be obtained from

$$\sigma_n = 2Re\{[\cos(n,y) - \mu_1\cos(n,x)]^2\ \varphi_{1k}'(z_1) + [\cos(n,y) - \mu_2\cos(n,x)]^2\ \varphi_{2k}'(z_2)\} \tag{6.7}$$

where

$$\cos(n,x) = \frac{dy}{ds}, \qquad \cos(n,y) = \frac{dx}{ds} \tag{6.8}$$

Savin presented the above theory for an infinite homogenous anisotropic plate weakened by a hole, the contour of which is given by

$$x = R(\cos\theta + \varepsilon\sum_{k=2}^{5} a_k\cos k\theta)$$
$$y = R(-c\sin\theta + \varepsilon\sum_{k=2}^{5} a_k\sin k\theta) \tag{6.9}$$

The solution presented is limited to the second approximation and a mapping function that consists of six terms. To improve these limitations is extremely difficult. It was attempted but later abandoned.

A computer program was written to calculate the mapping function and then to calculate the stress concentration around the rectangular hole. The material properties,

the aspect ratio and the radii of the corners of the rectangle and the loading (uniaxial or biaxial) can be altered in the program.

The mapping procedure used is elaborated on in Appendix A and the solution presented by Savin, and that which was used in the computer program is presented in Appendix B.

6.2 The finite element method [37,38,39]

The finite element method is a computer-aided mathematical technique for obtaining approximate solutions to a wide variety of engineering problems.

In the finite element method, the solution region or structure is built up of many small, interconnecting subregions or elements. These elements are interconnected at a finite number of points called the nodal points. If the force-displacement relationships for the individual elements are known, it is possible to derive the properties and study the behaviour of the structure.

The relationships between load, displacement, stress and strain are briefly outlined with specific reference to the quadratic isoparametric quadrilateral element. This is an eight-noded quadrilateral element with two degrees of freedom at each node.

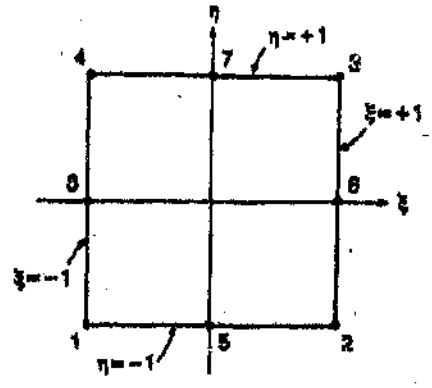


Figure 6.2 An eight-node quadratic isoparametric element [reference 37]

A shape function is chosen that defines the displacement at any point in the element in terms of the nodal displacements. The shape function for the element is quadratic since the three nodes on each side uniquely determine a quadratic, however, inside the element the shape function may vary cubically in some directions. The shape functions for the corner and midside nodes may be represented by those for node 1 and 5 respectively.

$$\phi_1(\xi,\eta) = \frac{1}{4}(1-\eta)(1-\xi)(-\eta-\xi-1)$$
$$\phi_5(\xi,\eta) = \frac{1}{2}(1-\xi^2)(1-\eta) \qquad (6.10)$$

The shape function automatically guarantees continuity of displacements with adjacent elements.

The term "isoparametric" in the description of the element refers to the fact that the order of both the geometry and the shape functions are the same. The geometry function is the function which determines the shape an edge of an element may take in modelling a curved boundary in a model.

The strain at any point in the element may be obtained by differentiation of the displacements. The form of differentiation will depend upon the type of problem since in plane elasticity, the strains are given by the first derivative whilst for bending problems, the strain is obtained from the curvature - the second derivative. Hence the strains may be related to the nodal displacements.

$$\{\varepsilon\} = [B]\begin{Bmatrix} u \\ v \end{Bmatrix} \tag{6.11}$$

The internal stresses $\{\sigma\}$ at any point are now related to the strains $\{\varepsilon\}$ at that point by the elasticity matrix [D]. The terms in [D] are different for each class of element, and whether the problem is plane stress or plane strain in plane elasticity problems, but in general [D] contains the material stiffness terms.

$$\{\sigma\} = [D]\{\varepsilon\} \tag{6.12}$$

Thus for each element, the state of stress is given in terms of the node displacements which are yet unknown.

$$\{\sigma\} = [D][B]\begin{Bmatrix} u \\ v \end{Bmatrix} \tag{6.13}$$

A solution for the displacements arises from a consideration of the virtual work produced by the forces at the element nodes and the strain-energy experienced by the element - the internal stresses $\{\sigma\}$ being replaced by statically equivalent nodal loads $\{F\}$. The total strain energy for the element is obtained from:

$$\begin{aligned}\delta U &= \int_v \{\varepsilon\}^T \{\sigma\}\, dV \\ &= \int_v [B]^T \begin{Bmatrix} u \\ v \end{Bmatrix}^T [D][B] \begin{Bmatrix} u \\ v \end{Bmatrix} dV\end{aligned} \tag{6.14}$$

where V is the volume of the element.

For the virtual work

$$\begin{aligned}\delta W &= \sum_{i=1}^{n} (F_{xi} u_i + F_{yi} v_i) \\ &= \begin{Bmatrix} u \\ v \end{Bmatrix}^T \begin{pmatrix} F_x \\ F_y \end{pmatrix}\end{aligned} \tag{6.15}$$

Equating the strain energy to the virtual work results in

$$\begin{aligned}\begin{pmatrix} F_x \\ F_y \end{pmatrix} &= \int_v [B]^T [D][B]\, dV \begin{Bmatrix} u \\ v \end{Bmatrix} \\ &= [K] \begin{Bmatrix} u \\ v \end{Bmatrix}\end{aligned} \tag{6.16}$$

Hence the element stiffness matrix is

$$[K] = \int_V [B]^T [D][B]\, dV \tag{6.17}$$

To obtain a complete solution the two conditions of displacement compatibility and equilibrium have to be satisfied throughout. Any system of nodal displacements for the whole structure in which all the elements participate automatically satisfies the first condition. As the conditions of overall equilibrium have already been satisfied within an element all that is necessary is to establish equilibrium conditions at the nodes of the structure. The resulting equations will contain the displacements as unknowns, and once these have been solved the structural problem is determined.

For a quadratic isoparametric quadrilateral, equation (6.16) consists of a set of 16 linear equations in which the displacements are the unknowns. The structural stiffness matrix can be obtained by the summation of all the element stiffness matrices in the structure. A loading system of applied forces and displacement constraints are placed at certain of the nodes.

Thus a system of equations is obtained for the entire region in terms of the unknown node displacements. This linear system of equations is solved for the displacements.

For each element, the node displacements are then used with equation (6.13) to obtain the state of stress.

The creation of a finite element model can be grouped into three distinct phases : preprocessing, solution and postprocessing.

Preprocessing phase - The data used to describe the physical problem is used to create data which is then used as input to the solution phase. The geometric details of the physical problem are entered to create a domain over which a mesh is generated. The material and physical properties are entered together with the loading and boundary conditions.

Solution phase - This entails extensive computation solving the system equations with data entered from the preprocessing phase.

Postprocessing phase - The postprocessor is used to filter out only the important data, and present and display it to the user in a concise manner.

The finite element package used was NISA. NISA (Numerically Integrated elements for System Analysis) is a general purpose finite element program developed by EMRC. A comprehensive library of linear and higher order isoparametric elements are available which include 3-D laminated composite shell elements. Linear isotropic and orthotropic elastic material models are also available.

A computationally efficient mesh would be one that achieves a desired accuracy in the area of interest, whilst using a minimum number of degrees-of-freedom (DOF) throughout the rest of the domain. This generally implies a greater DOF density in the areas of interest and lesser DOF densities elsewhere. Concave sections of a boundary with a small radius of curvature will produce locally, sharp increases in the stress solution. Since the maximum is expected to occur in the radius of the rectangle, a greater DOF density is necessary in order to maintain a given level of accuracy i.e. the mesh must be locally refined. This can be achieved by decreasing the size of the elements and not the order. Elements in a mesh should not be locally refined so much that the size of the smallest element is tiny in comparison with the largest element, as this tends to produce an ill-conditioned stiffness matrix. Abrupt changes in mesh refinement from fine to very coarse should generally be avoided; a gradual transition is generally more efficient.

Modelling errors may arise in an attempt to model curved boundaries. These errors are known as geometric errors. Non-polynomial curves for boundaries are impossible to match exactly using polynomial elements. These boundary mismatches change the domain of the problem since, in effect, the domain is defined by the outer boundary of the mesh elements. The most common non-polynomial curve is a circular arc. It is therefore recommended that curved boundaries be modelled with curve-sided elements (eg quadratics or higher order) whenever a solution is sought in the vicinity of the curved boundary.

6.2.1 The finite element model

Due to the symmetry of the problem, only one quarter of the plate was modelled.

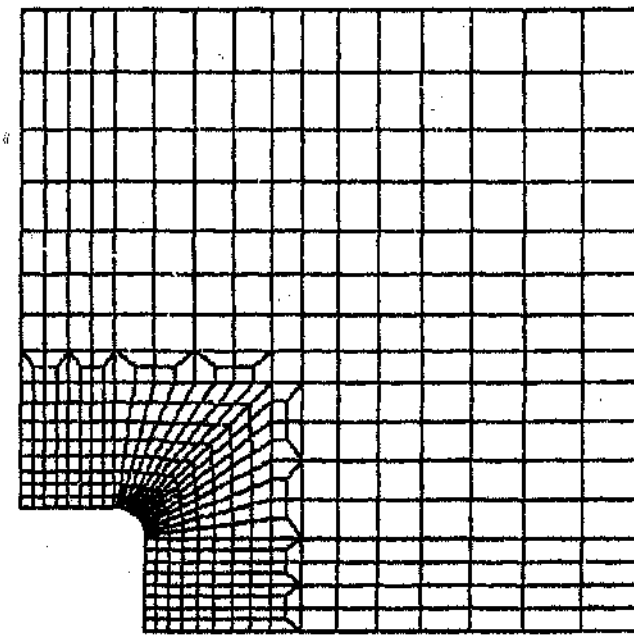


Figure 6.3 A typical finite element mesh of a plate with a rectangular hole.

A two dimensional, plane stress, quadratic, isoparametric, quadrilateral element was used and the size of the element was varied to obtain local mesh refinement around the rectangular opening. Material properties were entered as would be for an orthotropic material. A single force was applied to the midpoint of the upper edge of the plate, and all the nodes along the upper edge were constrained to have the same displacement as the loaded node to model the clamped edges. The model consists of 480 elements and 1537 nodes which results in a model with 3042 degrees of freedom.

6.3 Results

The results obtained from the theory of elasticity are presented in Table 6.1.

Table 6.1 Theory of elasticity results

Plate	Maximum stress concentration and position			Minimum stress concentration and position		
	Value	x	y	Value	x	y
0°	2.859	18.79	18.11	-3.044	9.63	20.07
00°/90°	3.593	19.27	14.26	-0.773	9.14	20.06

No results are presented for the ±45° plate due to limitations of the theory presented by Savin. These limitations are discussed in the following section.

The results obtained from the finite element method are presented in Table 6.2.

Table 6.2 Finite element method results

Plate	Maximum stress concentration and position			Minimum stress concentration and position		
	Value	x	y	Value	x	y
0°	2.985	19.02	17.98	-3.381	0	20
±45°	5.978	19.78	16.45	-0.617	0	20
0°/90°	3.585	19.98	15.49	-0.657	0	20

6.4 Discussion

Due to the high degree of mathematical complexity and mapping difficulties introduced by the anisotropic nature of the composite material, Savin[5] made three major assumptions in an attempt to obtain an approximation of the stress concentration around an rectangular opening.

- the mapping function was limited to six terms.
- the stress solution was limited to the second approximation.
- the roots of the characteristic equation for an orthotropic material were assumed to be purely imaginary.

The function that maps the interior of the unit circle to an infinite plate which contains the opening was assumed to consist of only six terms. A practical mapping procedure must be capable of a close approximation, not only to the profile but to its curvature of the opening. Savin[5] limited the mapping terms to six whilst Sobey[1] recommended that 30 to 40 mapping terms be taken to avoid errors in curvature which produce significant errors in the stress distribution around an opening in an isotropic plate.

A comparison between the maximum stress concentration factor around a rectangular hole of the same shape but in an isotropic plate determined using Savin's solution and that presented by Peterson[3] using Sobey's method is useful. The solution computed using six mapping terms, 3.10, is significantly lower than Sobey's 3.57. The finite element method gave a stress concentration of 3.49, but one must remember that the finite element model is a plate with finite dimensions.

If the results for a circular hole in an orthotropic plate are compared between Savin's solution and the exact solution presented by Lekhnitskii[4], no discrepancy is found. This stems from the fact that the mapping function of a circular hole consists of a single term.

The plane stress problem of the theory of elasticity can be reduced to the determination of a stress function which satisfies a fourth order differential equation. The characteristic equation for an orthotropic plate takes the form relative to the principal directional of elasticity of:

$$\mu^4 + (\frac{E_x}{G_{xy}} - 2\nu_{xy})\mu^2 + \frac{E_x}{E_y} = 0$$

Lekhnitskii proved that the characteristic equation could have either complex or purely imaginary roots, but could not have real roots in the case of an ideal elastic body. Savin assumed the roots were purely imaginary. This condition holds true for an isotropic material, the 0° and the 0°/90° plate but when the shear modulus term

becomes large, as in the case of the ±45° plate, the condition is no longer met. For the carbon prepreg used in this investigation the condition is met for symmetrical balanced laminates with a lay-up of ±θ° where θ varies from 0°-15° and from 75°-90°.

Both the finite element method and the theory of elasticity do not take material nonlinearities and material strengths into consideration when calculating stresses.

7 Correlation of results

The stress distribution around the rectangular holes in the 0°, 0°/90° and ±45° plates were calculated using the theory of elasticity, the finite element method and the method of reflective photoelasticity. The results are presented in the following figures.

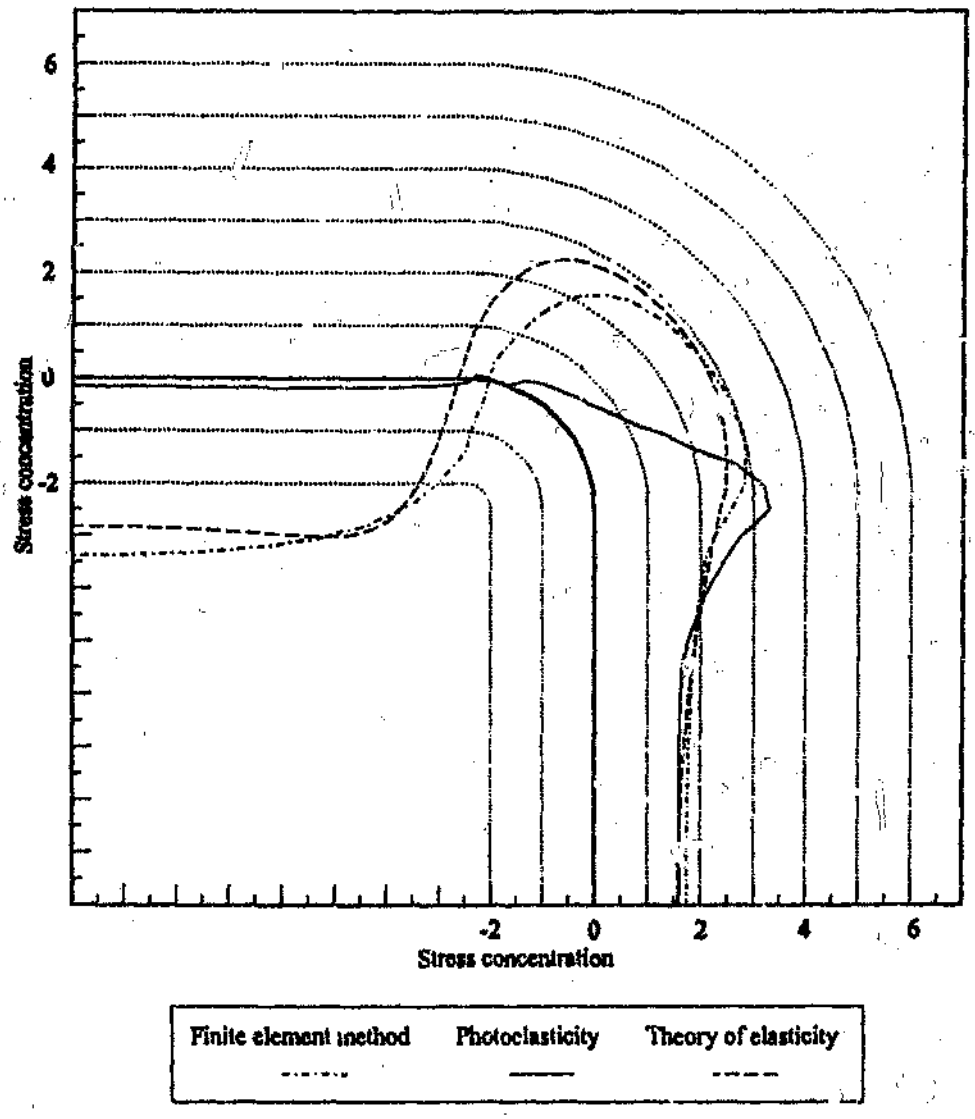


Figure 7.1 The stress distribution around the 0° plate

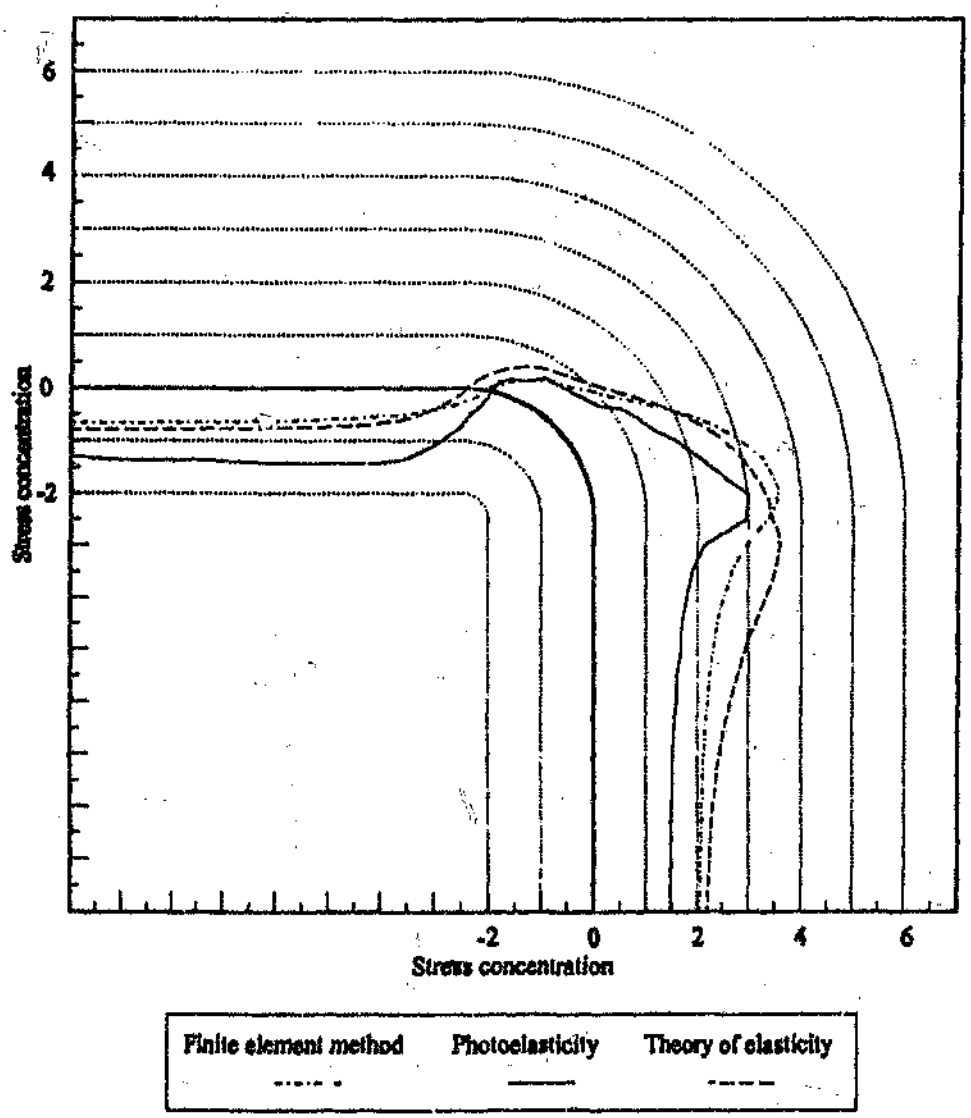


Figure 7.2 The stress distribution around the 0°/90° plate.

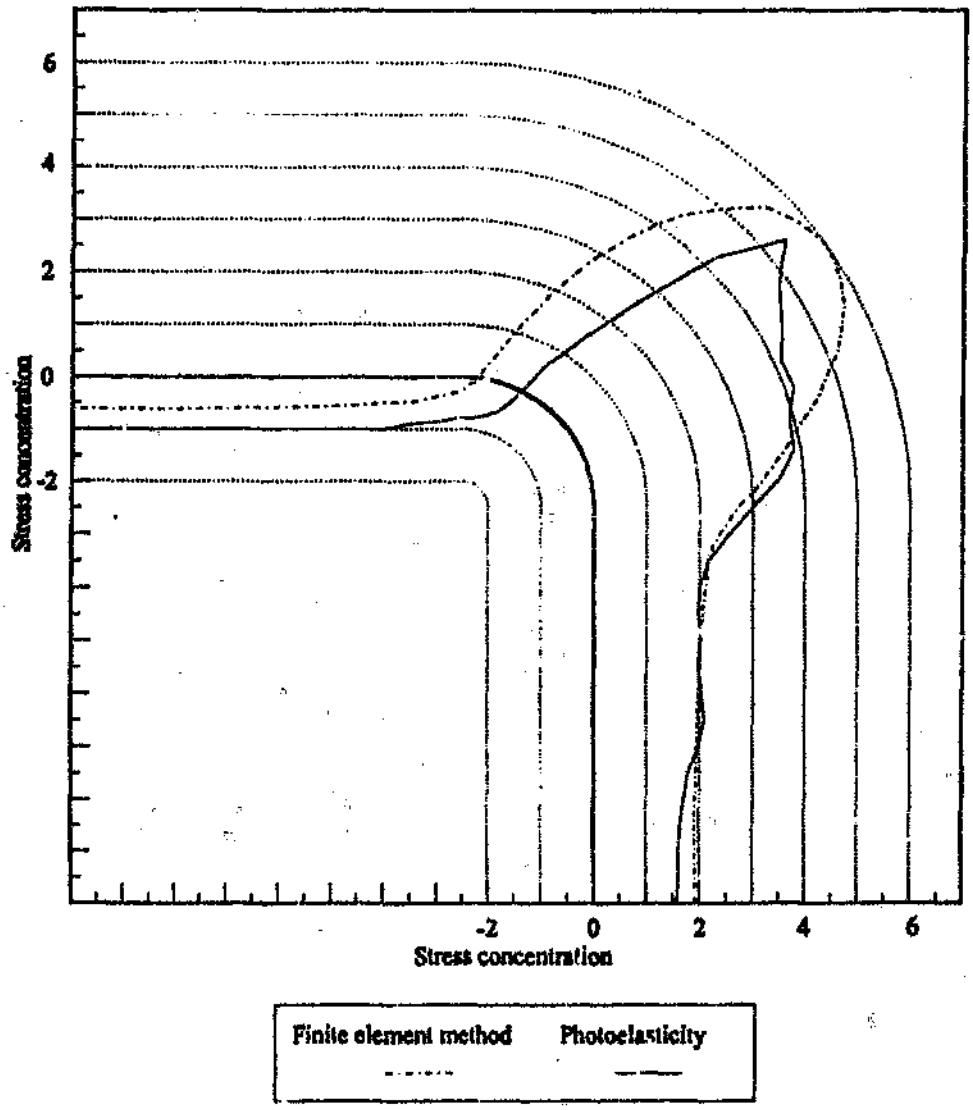


Figure 7.3 The stress distribution around the ±45° plate.

The stress distribution around the holes in the 0°/90° and ±45° plate, calculated using the finite element method and reflective photoelasticity, are plotted against the circumference of the hole. The x-axis on the plot begins at the intersection of the hole wi the x-axis and continues around to the intercept with the y-axis. The results are presented in the following figures.

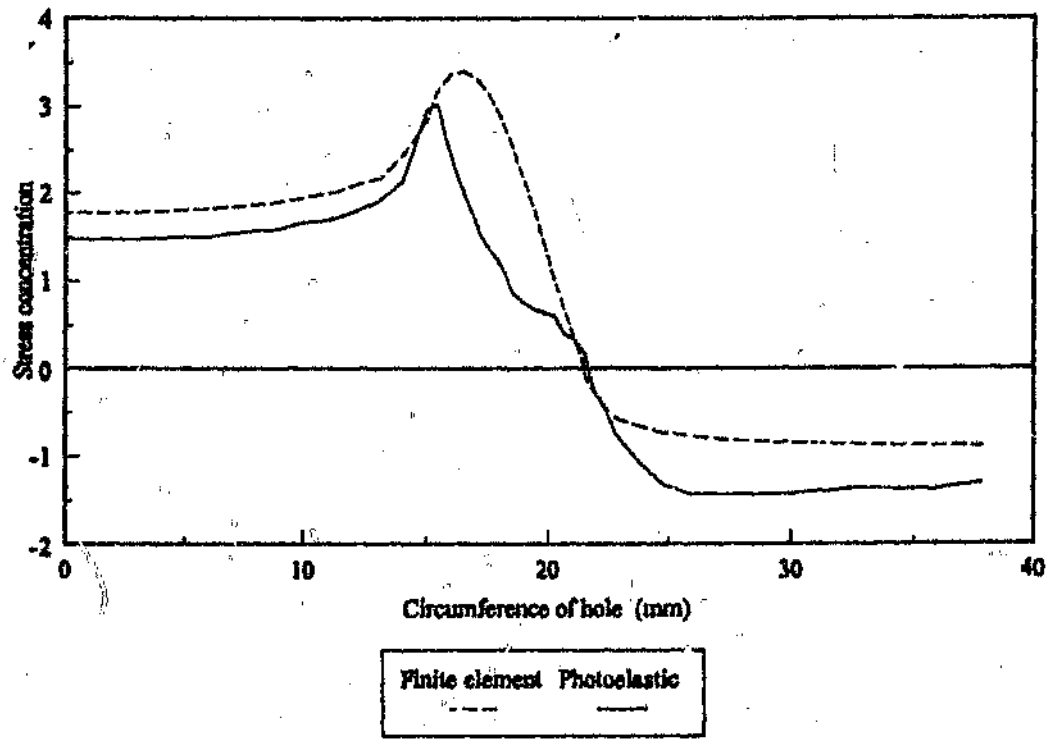


Figure 7.4 The stress distribution around the 0°/90° plate plotted versus the circumference of the hole

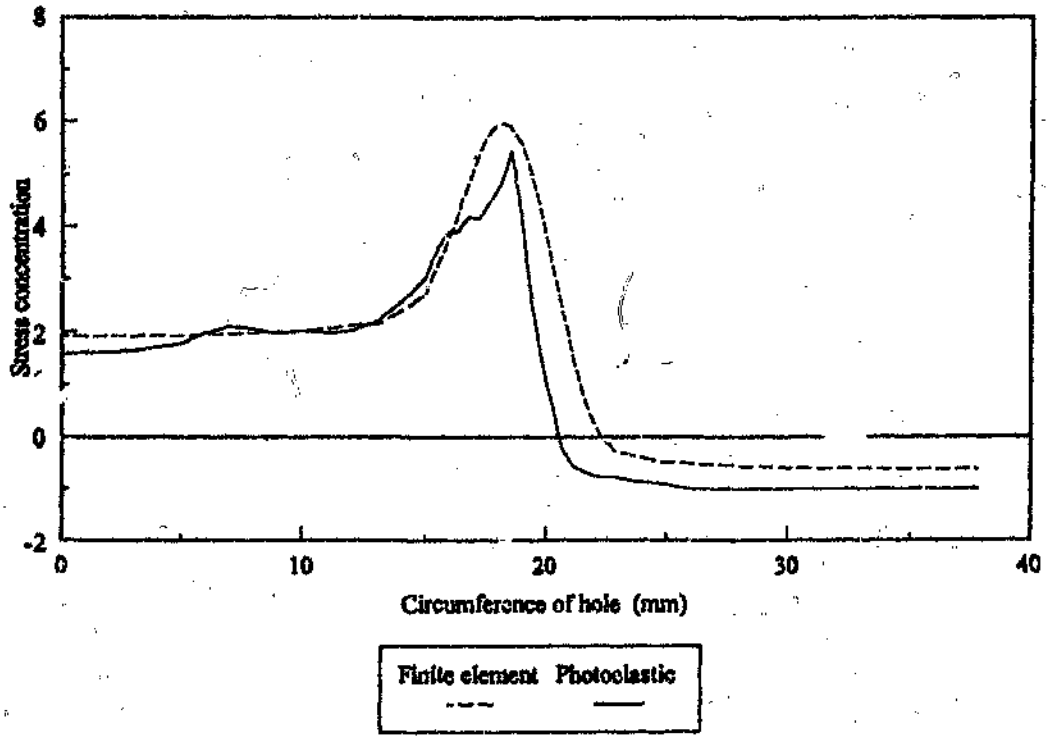


Figure 7.5 The stress distribution around the ±45° plate plotted versus the circumference of the hole

The correlation between the finite element results and those obtained from the theory of elasticity are good.

The correlation between the finite element and the photoelastic results are reasonably good for the 0°/90° and ±45° plate. The tensile stresses determined experimentally are lower in magnitude than those predicted using finite elements, however the compressive stresses are larger.

The correlation of the photoelastic results with the analytical for the 0° plate is poor as illustrated in Figure 7.1.

In an attempt to provide a possible explanation for the discrepancies in the finite element method and the photoelastic results, the plates were modelled in finite elements with possible modifications.

CASE 1:

Initially, the plate was modelled using plane-stress orthotropic elements in order to obtain a mesh resolution which was judged to be sufficiently refined around the stress concentration. The model had 480 elements. The stress distribution results calculated using the finite element method were generated using this model.

CASE 2:

The material properties, E_L, E_T and G_{LT} determined for the carbon preimpregnated fibres were the average obtained for five test specimens. In order to establish the effect a variation in the material properties would have on the stress concentration, the material properties were altered. The standard deviation was added to E_L to give 138.906 GPa, a standard deviation was subtracted from E_T to give 7.964 GPa and G_{LT} was calculated to be 4.384 GPa. The apparent elastic properties of the plates were now determined to be:

Table 7.1 Modified elastic properties of carbon plates.

Construction	E_{11} (GPa)	E_{22} (GPa)	G_{12} (GPa)	ν_{12}
[0°]	138.906	7.964	4.384	0.3
$[0°/90°]_s$	73.738	73.738	4.384	0.0325
$[\pm 45°]_s$	15.727	15.727	35.707	0.7937

CASE 3:

The edges of the carbon plates which were clamped had aluminium tabs to improve the grip. Two holes were drilled through the tab and plate to allow the grips to be bolted firmly closed. Under loading significant isochromatics were observed originating from these positions. It was surmised that the applied load was not adequately

transferred at this point and the plate was being "left behind" resulting in significant stresses. This was very noticeable in the 0° and the 0°/90° plate but not the ±45° plate. A reason for this could be the high ratio of the longitudinal modulus (E_{11}) to the shear modulus (G_{12}) of the 0° and the 0°/90° plates. The load is transferred to the rest of the plate over a greater distance than would occur in the ±45° plate which has a large shear modulus compared to the longitudinal modulus.

The upper row of nodes in the model, where the plate is clamped, are constrained to have identical displacements in the y-direction. In the attempt to model the effects of the boltholes, the constraints on three nodes were removed, effectively removing load from these nodes.

CASE 4:

In order to used a 3-D general shell element, which has more degrees of freedom compared to a plane-stress element, the mesh had to be replaced with a coarser mesh due to the limit of the number of degrees of freedom allowed in the finite element package. The new model had 340 element. Any variation in the stress concentration compared to case 1 is due to the coarser mesh.

Since a shell element was now being used, a 3-D laminated composite shell element could be employed since interlaminar shear stresses would be accounted for in the composite element. A comparison between the stress results of the initial plane-stress orthotropic element used and the composite elements was judged to be unsuitable due to the reduction in accuracy of the stresses resulting from the coarser mesh.

The results of the three modifications to the finite element model are listed in Table 7.1

Table 7.2 The results of a modified finite element model

		Case 1	Case 2	Case 3	Case 4	Experimental Results
0°	σ_{max}	2.985	2.956	2.986	2.932	3.304
	σ_{min}	-3.381	[illegible]	-3.384	-3.342	-0.155
0°/90°	σ_{max}	3.585	3.583	3.627	[illegible]	3.025
	σ_{min}	-0.657	-0.642	-0.667	-0.652	-1.367
±45°	σ_{max}	5.978	[illegible]	5.975	[illegible]	5.439
	σ_{min}	-0.617	[illegible]	-0.613	[illegible]	-1.000

The stress concentration for the 0° and ±45° plate is very sensitive to variations in material properties. This is particularly so for the 0° plate since a variation in the properties perpendicular to the fibre orientation has a substantial effect on the minimum stress concentration.

The results for the 0°/90° and the ±45° plate are affected by the resolution of the mesh. The coarser the mesh, the lower the calculated maximum stress concentrations.

The load applied to the plate may not have been symmetrically placed in the z-direction due to the aluminium tabs and the manner in which the plates were clamped in the grips. This would result in a moment about the x-axis (the axis parallel to the aluminium tabs). If the load was offset by 0.5mm, the stress concentration varies between the middle of the plate and the outer surfaces. These discrepancies are listed in Table 7.3.

Table 7.3 Variations in the stress concentration through the thickness of the plate.

	$\Delta \sigma_{max}$
0°	0.001
0°/90°	0.046
±45°	0.010

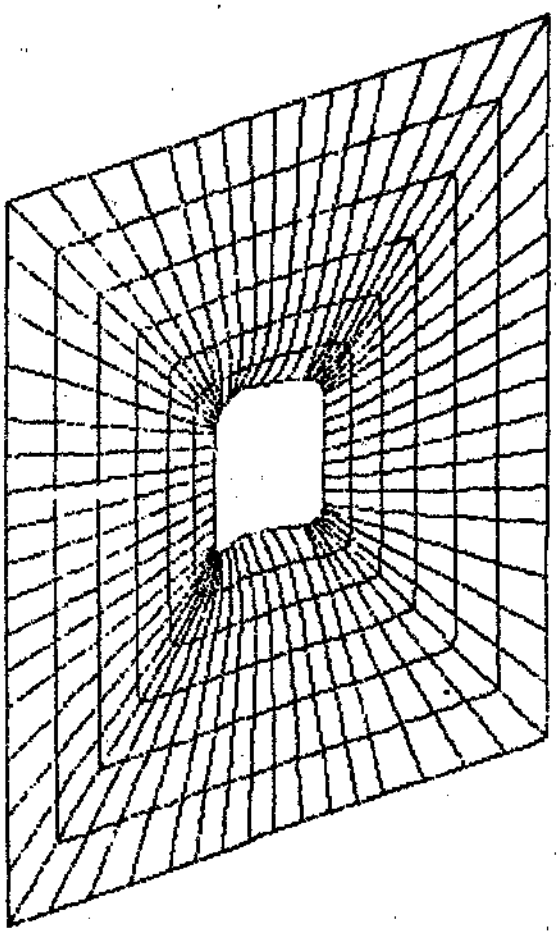
When a thin sheet containing an opening is subject to a unidirectional tensile loading, the region adjacent to the edge of the opening, perpendicular to the direction of loading, is in a state of compression. The presence of this compressive zone could result in local buckling which produces out of plane deflections.

In the case of the 0° plate, the transverse modulus, E_{22} is more than a factor of 14 lower than the longitudinal modulus, E_{11}. The finite element solution and theory of elasticity, which do not consider material nonlinearities, geometric imperfections or the material strength, both predicted compressive stress concentrations greater than 3. The load applied to the plate to obtain the photoelastic solution was 20 kN, i.e. a stress of approximately 62 MPa. According to the formula for stress concentration,i.e. the maximum stress divided by the applied stress, the plate experienced a stress of more than 200 MPa in the transverse direction. The compressive strength of a unidirectional carbon prepreg is in the region of 140 MPa, hence the plate was theoretically stressed to failure. However, the plate did not fail and therefore it is concluded that it must have experienced out of plane deformations.

The 0° plate was modelled in finite elements in order to verify the buckling hypothesis. A coarse mesh was generated consisting of only 96 elements due to a severe limitation in the degrees-of-freedom of the finite element package used. Using this model, a static analysis was performed to obtain the stress distribution. The maximum compressive stress concentration predicted using this model was 2.677. A buckling analysis was then performed to obtained a buckling load of 52 kN. The buckling mode is illustrated in Figure 7.6.



Top view



Rotated view of buckled plate



Side view

Figure 7.6 Buckling mode shape of the 0°plate

The finite element model has a coarse mesh resulting in lower stress concentrations, and it can be surmised that a finer mesh would result in a lower buckling load. The finite element analysis does not take into account material nonlinearities and geometric imperfections which would result in out-of-plane deflections of the plate.

To confirm the buckling hypothesis, the 0° plate was placed in the testing machine. A straight edge was used to judge the curvature of the plate, which initially was flat. A load of 20 kN was applied and there was significant out-of-plane distortion, to the extent that the straight edge could now be "rocked" over the bulge.

The 2mm thick photoelastic coating would detect this out-of-plane distortion and this could explain the discrepancy between the analytical and experimental results for the 0° plate.

7.1 Synopsis

The use of transmissive photo-orthotropic-elasticity as an effective design tool is limited by the photo-orthotropic material available. The material needs to be improved in terms of its photoelastic sensitivity and fringe resolution characteristics, in order to obtain sufficient well -defined fringes to make accurate stress magnitude predictions possible. To conduct a stress analysis of a structure, a model needs to be constructed from the photo-orthotropic material. The material properties are therefore limited to those of the model material. Thus, transmissive photoelasticity is an arkward design tool.

Reflective photoelasticity is an effective experimental method capable of determining stress magnitudes at the boundary of an orthotropic material. Since a reflective coating can be applied directly to a prototype, no model needs to be built for the analysis, making reflective photoelasticity a practical design tool. Since no model needs to be built, the method is independent of the material of the structure being analysed, however, the material properties need to be accurately determined since the stress concentration factors calculated using analytical methods may be sensitive to variations in the material properties. This sensitivity was illustrated in the analysis of the ±45° plate.
Care needs to be taken to ensure unexpected out-of-plane distortions do not occur in a plane-stress analysis since these will be detected by the coating and the results ruined, as was the case for the localised buckling of the 0° plate.

The correlation of the stress concentrations calculated analytically using the finite element method and the theory of elasticity were good. The solution for the stress concentrations around an opening in an orthotropic material using the theory of elasticity presented by Savin[5], is limited by the assumptions made viz.:

- the mapping function is limited to six terms.
- the stress solution is limited to the second approximation.
- the roots of the characteristic equation for an orthotropic material were assumed to be purely imaginary.

The third approximation limited the solution and no results could be obtained for the ±45° plate. Despite this, the solutions obtained for the other plates compared well with the finite element solution. The limitations placed on the theory of elasticity solution need to be eliminated since a rapid approximation to the stress concentrations around any rectangular hole with rounded corners can be obtained using this method.

It must always be remembered however, that the analytical methods used assume perfectly linear elastic responses. The analyses do not take any geometric imperfections or the material strength into consideration. This became evident in the 0° plate, when the maximum compressive stress calculated was greater than the compressive strength of the material, resulting in localised buckling of the plate.

8 Conclusions

The experimental and theoretically derived stress concentration factors were determined and their correlation generally was good.

Care must be taken to consider the theoretical results obtained since material limitations and geometric imperfections are usually not considered. The feasibility of the theoretical results should be investigated.

The use of transmissive photoelasticity is limited by the materials available and as a practical experimental stress analysis technique it is also limited since a model is required.

Photoelastic coatings can be effectively employed as an experimental method to solve numerous plane stress-analysis problems involving composite materials. A major advantage of the birefringent coating is that since the coating can be applied directly to a prototype, the need for a model is eliminated. The variations in the elastic constants of an orthotropic fibre-reinforced material with direction must be taken into account in an analysis since these materials present characteristics quite different to isotropic materials.

9 Recommendations

Savin[5] made three major assumptions in an attempt to obtain an approximation of the stress concentration around an rectangular opening.

- the mapping function was limited to six terms.
- the stress solution was limited to the second approximation.
- the roots of the characteristic equation for an orthotropic material were assumed to be pu ly imaginary.

The theoretical solution of an opening in an orthotropic mat ial using the theory of elasticity needs to be extended to eliminate the limitations placed on the solution.

The following problems concerning the appli ion of birefringent coatings need to be investigated.

- the influence the interlaminar shear stresses on the boundary have on the isochromatics.
- the effect of Poisson's ratio mismatch.

The adhesive layer may influence the magnitude of the edge isochromatic fringe order since it provides a shear-lag region which may influence the state of strain in the coating. It has been determined[14] that this effect is not significant for most isotropic applications. The effect of the adhesive layer on a composite material needs to be investigated.

10 References

1. Sobey A.J., The Estimation of Stresses Around Unreinforced Holes in Infinite Elastic Sheets, *Reports & Memoranda*, Report 3354, October 1962.

2. Sobey A.J., Stress-Concentration Factors for Rounded Rectangular Holes in Infinite Sheets, *Reports & Memoranda*, Report 3407, November 1963.

3. Peterson, R.E., *Stress Concentration Factors*, John Wiley and Sons, New York, 1973.

4. Lekhnitskii S.G., *Anisotropic Plates*, Translated from the Russian 2nd Edition by S.W. Tsai and T. Cheron, Gordon and Breach Science Publishers, 1968.

5. Savin G.N., Stress Distribution around Holes, *NASA Technical Translation F-607*, November 1970.

6. Green A.E., Stress Systems in Isotropic and Aeolotropic Plates V, *Royal Society of London Proceedings A*, Volume 184, 1945.

7. Sampson R.C., A Stress-Optic Law for Photoelastic Analysis of Orthotropic Composites, *Experimental Mechanics*, Volume 10, No. 1, May 1970, pp. 210-215.

8. Dally J.W., Prabhakaran R., Photo-Orthotropic-Elasticity, *Experimental Mechanics*, Volume 11, No. 8, August 1971, pp. 346-356.

9. Daniel I.M., Koller G.M., Niiro T., Development and Characterization of Orthotropic-birefringent Materials, *Experimental Mechanics*, Volume 24, No. 2, June 1984, pp 135-143.

10. Prabhakaran R., Fabrication of Birefringent Anisotropic Model Materials, *Experimental Mechanics*, Volume 20, No. 9, September 1980, pp. 320-321.

11. Hyer M.W., Liu D.H., An Assessment of the Accuracy of Orthotropic Photoelasticity, *NASA Contractor Report 3773*, March 1984.

12. Prabhakaran R., Photoelastic Investigation of Bolted Joints in Composites, *Composites*, July 1982, pp. 253-256.

13. Dally J.W., Alfirevich I., Application of Birefringent Coatings to Glass-fiber-reinforced Plastics, *Experimental Mechanics*, Volume 9, No. 3, March 1969, pp. 97-102.

14. Pipes R.B., Dally J.W., On the Birefringent-coating Method of Stress Analysis for Fiber-reinforced Laminated Composites, *Experimental Mechanics*, Volume 12, No. 6, June 1972, pp 272-277.

15. Rowlands R.E., Daniel I.M., Whiteside J.B., Stress and Failure Analysis of a Glass-Epoxy Composite Plate with a Circular Hole, *Experimental Mechanics*, Volume 13, No. 1, January 1973, pp. 31-37.

16. Koshide S., Strain Analysis along the Curved Boundary of Composites by the Birefringent-Coating Method, *Experimental Techniques*, Volume 10, No. 11, November 1986, pp. 20-23.

17. Daniel I.M., Rowlands, R.E., Whiteside J.B., Effects of Material and Stacking Sequence on Behavior of Composite Plates with Holes, *Experimental Mechanics*, Volume 14, No. 1, January 1974, pp. 1-9.

18. Dally J.W., Riley W.F., *Experimental Stress Analysis*, 2nd edition, McGraw-Hill Book Company, 1978.

19. Heywood R.B., *Photoelasticity for Designers*, 1st Edition, Pergamon Press, London, 1969.

20. Post D., Photoelasticity, *Experimental Mechanics*, volume 19, no. 5, May 1979, pp 176-192.

21. Kobayashi A., *Handbook on Experimental Mechanics*, Society for Experimental Mechanics Inc, Prentice-Hall Inc, 1st Edition, 1987.

22. Cernosek J., On Photoelastic Response of Composites, *Experimental Mechanics*, Volume 15, No. 9, September 1975, pp. 354-357.

23. Pipes R.B., Dalley J.W., On the Fiber-reinforced Birefringent Composite Materials, *Experimental Mechanics*, Volume 13 No.8. August 1973 pp 348-349.

24. Doyle P., Watts S., *Refractive Index Matching of Glass and Plastic Components in a Fibreglass Composite*, Physics IIC Project Report, University of the Witwatersrand, Octob[illegible]

25. Holister G.S., *Developments in Composite Materials - 2 Stress Analysis*, Applied Science Publishers, London, 1981.

26. *Instruction Manual for Model 241 Polariscope*, Photolastic Inc. Measurements Group.

27. Zandman F., Redner S.S., Riegner E.I., Reinforcing Effect of Birefringent Coatings, *Experimental Mechanics*, Vol. 2. No. 1, February 1962, pp. 55-63.

28. Jones R.M., *Mechanics of Composite Materials*, Scripta Book Company, Washington D.C., 1975.

29. Post D., Zandman F., Accuracy of Birefringent-coating Method for Coatings of Arbitrary Thickness, *Proceedings of the Society for Experimental Stress Analysis*, Vol. XVIII, No. 1, January 1960, pp. 21-32.

30. Technical Data Bulletin T-401, *How to Select Photoelastic Coatings*, Photolastic Inc. Measurements Group, 1975.

31. Measurements Group Tech Note, *TN-704 How to Select Photoelastic Coatings*, Measurements Group Inc, 1978.

32. Instruction Bulletin IB-222 D, *Instructions for Bonding Flat and Contoured Photoelastic Sheets to Test Surfaces*, Photolastic Division Measurements Group Inc, 1982.

33. Bulletin S-116-D, *Materials For Photoelastic Coatings & Photoelastic Models*, Photolastic Division Measurements Group Inc, 1983.

34. Measurements Group Tech Note, *TN-706 Corrections to Photoelastic Coating Fringe-Order Measurements*, Measurements Group Inc, 1982.

35. *Operating Instructions and Technical Manual - Strain Measurement with the 030-Series Reflection Polariscope*, Photolastic Division Measurements Group, 1977.

36. Measurements Group Tech Note, *TN-702 Introduction to Stress Analysis by the PhotoStress Method*, Measurements Group Inc, 1981.

37. Rockey K.C., Evans H.R., Griffiths D.W., Nethercot D.A., *The Finite Element Method - A Basic Introduction for Engineers*, 2nd edition, Granada, 1983.

38. Burnett D.S., *Finite Element Analysis - From Concept to Application*, Addison-Wesley Publishing Company, 1987.

39. Zienkiewicz O.C., *The Finite Element Method in Engineering Science*, 2nd edition, McGraw-Hill, London, 1971.

Appendix A
The mapping problem

A Mapping [1]

Difficulties arise in the mapping of contours in accurately reproducing the profile and curvature distribution at all points on the boundary. A practical mapping procedure must be capable of a close approximation not only to the profile but to its curvature. Exact agreement with the desired profile may require an infinite number of terms in the mapping function, as, for example, when a curvature discontinuity is present. Generally it is found necessary to take 30 - 40 terms to avoid errors in curvature which produce significant or even serious errors in the stress.

A.1 The mapping problem

For any given hole in an infinite sheet there exists an unknown mapping function $z = m(\zeta)$ which exactly maps the boundary C of the hole onto the unit-circle in the ζ-plane. If we assume the tangent to C is continuously turning at all points of the boundary, the transformation is free from singularities on the boundary and the mapping function $m(\zeta)$ can be expressed in the form of a power series in ζ

$$z = \sum_{m=0}^{M} b_m \zeta^{1-m} \tag{A.1}$$

or in parametric form

$$z(\theta) = x(\theta) + iy(\theta) = \sum_{m=0}^{M} b_m \, e^{(1-m)i\theta} \tag{A.2}$$

The profile C is assumed symmetric about the x- and y-axes, so that all the mapping co-efficients b_m are real and for odd values of m they are zero.

A.2 Melentiev's iterative procedure for finding the mapping co-effients

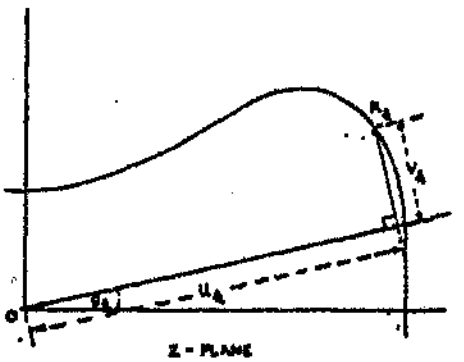
Using Melentiev's procedure outlined in reference 1, b_m is computed from the reduced variable

$$\frac{z}{\zeta} = u(\theta) + iv(\theta) = \sum_{m=0}^{M} b_m \zeta^{-m} \tag{A.3}$$

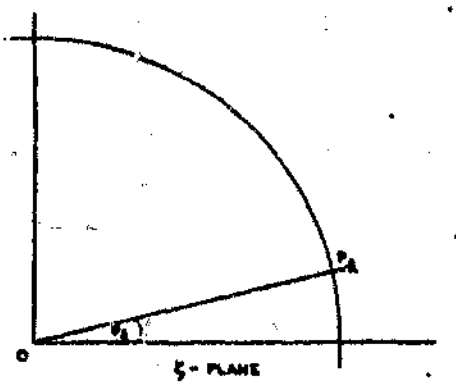
As ζ goes aroun the unit circle, $u(\theta)$ and $v(\theta)$ are given by

$$u(\theta) = \sum_{m=0}^{M} b_m \cos m\theta$$

$$v(\theta) = -\sum_{m=1}^{M} b_m \sin m\theta \tag{A.4}$$



(a)



(b)

Figure A.1 Co-ordinate system used in the Melentiev process

Appendix A

If a set of (K+1) points $P_0, P_1....P_K$ is selected on the unit circle in the ζ-plane. Under the mapping, each point P_k (k = 0 to K) corresponds exactly with a point Q_k of C. In order to obtain the mapping co-efficients b_m it is necessary to estimate the positions of the points Q_k on C. The procedure must allow for the initial ignorance of the points Q_k and only tentative estimates of Q_k, say R_k, can be made.

The (K+1) points P_k are chosen to equally subdivide the first quadrant so

$$\theta_k = \frac{K\pi}{2K} \qquad k=0,1,...K \tag{A.5}$$

The extreme value of u, namely u_0 and u_K are known and the remaining (K-1) functions u_k are initially estimated. The equations which determine b_m are taken to be

$$u_k = \sum_{m=0}^{M} b_m \cos m\theta_k \tag{A.6}$$

where there must be at least as many b_m's as there are values of u_k.

If M = 2K with θ_k equally spaced, these equations can be solved exactly without matrix inversion to give

$$\begin{aligned} b_0 &= \frac{1}{2K}\{ u_0 + 2u_1 + 2u_2 + ... + 2u_{K-1} + u_K \} \\ b_{2m} &= \frac{1}{2K}\{ 2u_0 + \sum_{k=1}^{K-1} 4u_k \cos\frac{mk\pi}{K} + 2(-1)^m u_K \} \\ b_{2K} &= \frac{1}{2K}\{ u_0 - 2u_1 + 2u_2 ... + (-1)^{K-1}2u_{K-1} + (-1)^K u_K \} \end{aligned} \tag{A.7}$$

with all $b_{2m+1} = 0$.

The v_k's can now be computed and R_k found. Corrections of points R_k to R_k' nearer to C is now performed in order to establish a better estimate for u_k.

The discrepancy between C and C' at the reference points R_k is measured by

$$\delta = \sqrt{\sum_{k=0}^{K} \{(\delta x_k)^2 + (\delta y_k)^2\}} \tag{A.8}$$

If δ is reduced to about 10^{-5}, further iterations will produce no significant changes in the curvature variation of C'.

A computer program was written which calculated the mapping function with as many mapping coefficients as required.

References

1. Sobey A.J., The Estimation of Stresses around Unreinforced Holes in Infinite Elastic Sheets, *Reports & Memoranda* Report 3354, October 1962.

Appendix B

Theory of elasticity

B Theory of elasticity solution

The following an extract from Savin[1] pages 328 - 333.

"We will analyze an infinite homogeneous anisotropic plate weakened by a hole, the contour of which is given by equations

$$\begin{aligned} x &= R(\cos\theta + \varepsilon\sum_{k=2}^{5} a_k \cos k\theta) \\ y &= R(-c\sin\theta + \varepsilon\sum_{k=2}^{5} a_k \sin k\theta) \end{aligned} \tag{B.1}$$

The function that conformally maps the interior of the unit circle on an infinite area with the examined hole (B.1) consists of six terms and has the form

$$z = \omega(\zeta) = R\left(\frac{1-c}{2}\zeta + \frac{1+c}{2}\frac{1}{\zeta} + \varepsilon\sum_{k=2}^{5} a_k \zeta^{-k}\right) \tag{B.2}$$

The choice of the mapping functions (B.2) permits us to obtain quite easily the formulas for determining the stress state in a plane with various holes.

Let the contour of a hole be free of external forces, and let, at infinity, uniformly distributed forces of tension p, parallel to the Ox axis, and forces q, parallel to the Oy axis, act on the plate.

The solution of the problem of the stress state of a plate is found by combining two stress fields:

1 - the stress field that develops in a thick plate

$$\sigma_x^0 = p, \quad \sigma_y^0 = q, \quad \tau_{xy}^0 = 0 \tag{B.3}$$

In this case the projections of the forces acting on the contour of the assumed hole have the form

2 - the stress field occurring in a plate with a hole, to the contour of which are applied the forces

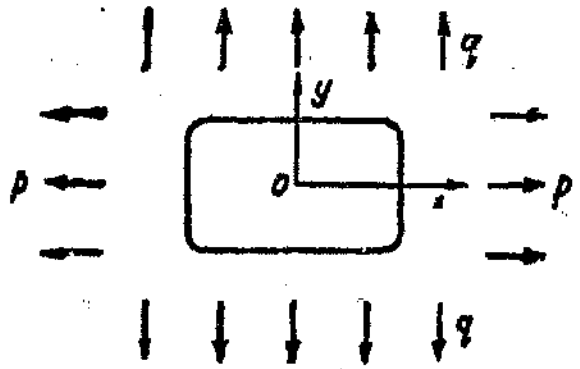


Figure B.1 Loading on the plate.

$$X_n^0 = -p\frac{dy}{ds}, \qquad Y_n^0 = q\frac{dx}{ds} \tag{B.4}$$

$$\begin{aligned} X_n &= -X_n^0 = p\frac{dy}{ds} \\ Y_n &= -Y_n^0 = -q\frac{dx}{ds} \end{aligned} \tag{B.5}$$

there being no forces at infinity.

We will determine the stress state of a plate when forces X_n, Y_n act on the contour.

The boundary values are represented in the form

$$\begin{aligned} -\int_0^s Y_n ds + C_1 &= \sum_{k=0} p_{1k}\sigma^k = p_{10} + \varepsilon p_{11} \\ \int_0^s X_n ds + C_2 &= \sum_{k=0} p_{2k}\sigma^k = p_{20} + \varepsilon p_{21} \end{aligned} \tag{B.6}$$

where

$$\begin{aligned} p_{10} &= -\frac{qR}{2}(\sigma + \frac{1}{\sigma}), \qquad p_{11} = -\frac{qR}{2}\sum_{k=2}^{5} a_k(\sigma^k + \frac{1}{\sigma^k}) \\ p_{20} &= -\frac{pRi}{2}c(\sigma - \frac{1}{\sigma}), \qquad p_{21} = \frac{pRi}{2}\sum_{k=2}^{5} a_k(\sigma^k - \frac{1}{\sigma^k}) \end{aligned} \tag{B.7}$$

Appendix B

In solving this problem we will confine ourselves to the second approximation. We will assume that the complex parameters for an orthotropic plate are purely imaginary ($s_1 = i\beta_1$, $s_2 = i\beta_2$). We will confine ourselves to the determination of the functions $\varphi(z_1)$ and $\psi(z_2)$ for the points of the contour of the given hole.

By using the theory outlined above, after several transformations we obtain

$$\varphi(\sigma) = \frac{R}{2}\left[N_0\sigma + \varepsilon\sum_{k=1}^{5}(N_k\sigma^k + N_{-k}\sigma^{-k}) + \varepsilon^2\sum_{k=1}^{7}(A_k\sigma^k + A_{-k}\sigma^{-k})\right] \tag{B.8}$$

Here we introduce the definitions:

$$\begin{aligned}
N_0 &= \frac{1}{\beta_1 - \beta_2}m_1 \\
N_{-1} &= -\frac{1}{\beta_1 - \beta_2}\delta_1(a_3 + \chi_1 a_5)m_1 \\
N_{-2} &= -\frac{1}{\beta_1 - \beta_2}\delta_1 a_4 m_1 \\
N_{-3} &= -\frac{1}{\beta_1 - \beta_2}\delta_1 a_5 m_1 \\
N_{-4} &= N_{-5} = 0
\end{aligned} \tag{B.9}$$

$$\begin{aligned}
N_1 &= \frac{1}{(\beta_1 - \beta_2)^2}[2\beta_2\delta_2(a_3 + \chi_2 a_5)m_2 - (\beta_1 + \beta_2)\delta_1(a_3 + \chi_1 a_5)m_1] \\
N_2 &= \frac{1}{(\beta_1 - \beta_2)^2}[2\beta_2\delta_2 a_4 m_2 - (\beta_1 + \beta_2)\delta_1 a_4 m_1 + (\beta_1 - \beta_2)a_2 n1] \\
N_3 &= \frac{1}{(\beta_1 - \beta_2)^2}[2\beta_2\delta_2 a_5 m_2 - (\beta_1 + \beta_2)\delta_1 a_5 m_1 + (\beta_1 - \beta_2)a_3 n_1]
\end{aligned} \tag{B.10}$$

$$\begin{aligned}
N_4 &= \frac{1}{\beta_1 - \beta_2}a_4 n_1 \\
N_5 &= \frac{1}{\beta_1 - \beta_2}a_5 n_1
\end{aligned}$$

Appendix B

$$A_{-1} = \delta_1[-3a_3N_3 - 2a_4N_2 - (a_3 + \chi_1 a_5)N_1 + \frac{\delta_1}{\beta_1 - \beta_2}(a_2^2 + 4\chi_1 a_2 a_4 + 2\chi_1 a_3^2 + 7\chi_1^2 a_3 a_5 + 4\chi_1^2 a_4^2 + 6\chi_1^3 a_5^2)m_1]$$

$$A_{-2} = \delta_1[-2a_5N_2 - a_4N_1 + \frac{\delta_1}{\beta_1 - \beta_2}(2a_2a_3 + 4\chi_1 a_2 a_5 + 5\chi_1 a_3 a_4 + 9\chi_1^2 a_4 a_5)m_2]$$

$$A_{-3} = \delta_1[-a_5N + \frac{\delta_1}{\beta_1 - \beta_2}(2a_2a_4 + a_3^2 + 5\chi_1 a_3 a_5 + 3\chi_1 a_4^2 + 5\chi_1^2 a_5^2)m_2]$$

$$A_{-4} = \frac{\delta_1^2}{\beta_1 - \beta_2}(2a_2a_5 + 2a_3a_4 + 6\chi_1 a_4 a_5)m_1$$

$$A_{-5} = \frac{\delta_1^2}{\beta_1 - \beta_2}(2a_3a_5 + a_4^2 + 3\chi_1 a_5^2)m_1$$

$$A_{-6} = \frac{\delta_1^2}{\beta_1 - \beta_2}2a_4a_5m_1$$

$$A_{-7} = \frac{\delta_1^2}{\beta_1 - \beta_2}a_5^2m_1 \qquad \text{(B.11)}$$

$$A_k = \frac{1}{\beta_1 - \beta_2}[(\beta_1 + \beta_2)A_{-k} + 2\beta_2 B_{-k}] \qquad (k = 1,...,7) \qquad \text{(B.12)}$$

Thus

$$m_1 = -pc + q\beta_2, \qquad n_1 = p + q\beta_2$$
$$m_2 = -pc + q\beta_1, \qquad n_2 = p + q\beta_1 \qquad \text{(B.13)}$$
$$\chi_p \quad \frac{1 - c\beta_p}{1 + c\beta_p}, \qquad \delta_p = \frac{1 - \beta_p}{1 + c\beta_p} \qquad (p = 1,2)$$

The co-efficients B_{-k} and B_k are found from A_{-k} and A_k if, in the latter, we substitute β_1, δ_1, κ_1, m_1 and n_1 respectively by β_2, δ_2, κ_2, m_2 and n_2, and conversely.

The function $\varsigma(\sigma)$ is found from (B.8), if, in the expressions of coefficients (B.9) and

Appendix B

(B.10) we perform circular permutation of the subscript i in β_i, δ_i, $\varkappa_i$, m_i and n_i (i = 1,2).

The expression for the normal stress acting on the areas normal to the contour of the hole acquire the form

$$\begin{aligned}\sigma_\theta = p\{&\frac{B^2}{C^2} + \frac{A^2}{C^2L}[A^4\beta_1^2 + A^2B^2(2\beta_1^2 + 1 - \beta_1^2\beta_2^2) + B^4(2 - \beta_2^2)] \\ &+ \frac{(\beta_1 + \beta_2)C^2}{L}(B\varphi_1 - B_1A\psi_1)\} \\ + q\{&\frac{A^2}{C^2} + \frac{B^2}{C^2L}[A^4\beta_1^2(2\beta_2^2 - 1) + A^2B^2(2\beta_2^2 - 1 + \beta_1^2\beta_2^2) + B^4\beta_2^2] \\ &+ \frac{(\beta_1 + \beta_2)B_2C^2}{L}(B\varphi_2 - \beta_1A\psi_2)\}\end{aligned} \tag{B.14}$$

Here we introduce the following definitions

$$\begin{aligned}A &= -c\cos\theta + \varepsilon\sum_{k=2}^{5} ka_k\cos k\theta \\ B &= \sin\theta + \varepsilon\sum_{k=2}^{5} ka_k\sin k\theta \\ C^2 &= A^2 + B^2 \\ L &= (A^2\beta_1^2 + B^2)(A^2\beta_2^2 + B^2)\end{aligned} \tag{B.15}$$

$$\begin{aligned}\varphi_1 &= -B + (1 + c)\sin\theta \\ &- \frac{2\beta_1 c}{\beta_1 - \beta_2}\left[\varepsilon\sum_{k=1}^{5} k(\delta_1 M_k - \delta_2\frac{\beta_2}{\beta_1}p_k)\sin k\theta - \varepsilon^2\sum_{k=1}^{7} k(\delta_1^2 A_{1k} - \delta_2^2\frac{\beta_2}{\beta_1}B_{1k})\sin k\theta\right] \\ \psi_1 &= A + \frac{2\beta_2 c}{\beta_1 - \beta_2}\left[\varepsilon\sum_{k=1}^{5} k(\delta_1 M_k - \delta_2 p_k)\cos k\theta - \varepsilon^2\sum_{k=1}^{7} k(\delta_1^2 A_{1k} - \delta_2^2 B_{1k})\cos k\theta\right]\end{aligned} \tag{B.16}$$

Appendix B

$$\varphi_2 = -B + \frac{2\beta_1}{\beta_1 - \beta_2}\left[\varepsilon\sum_{k=1}^{3} k(\delta_1 M_k - \delta_2 p_k)\sin k\theta - \varepsilon^2\sum_{k=1}^{7} k(\delta_1^2 A_{2k} - \delta_2^2 B_{2k})\sin k\theta\right]$$

$$\psi_2 = A + (1+c)\cos\theta - \frac{2\beta_2}{\beta_1 - \beta_2}\left[\varepsilon\sum_{k=1}^{3} k(\delta_1 M_k - \delta_2\frac{\beta_1}{\beta_2}p_k)\cos k\theta - \varepsilon^2\sum_{k=1}^{7} k(\delta_1^2 A_{2k} - \delta_2^2\frac{\beta_1}{\beta_2}B_{2k})\cos k\theta\right] \quad \text{(B.17)}$$

Hence

$$\begin{aligned} M_1 &= a_3 + \chi_1 a_5 \\ M_2 &= a_4 \\ M_3 &= a_5 \end{aligned} \quad \text{(B.18)}$$

$$\begin{aligned} A_{11} &= a_2^2 + 4a_2a_4\chi_1 + 2a_3^2\chi_1 + 7a_3a_5\chi_1^2 + 4a_4^2\chi_1^2 + 6a_5^2\chi_1^3 \\ &\quad + \frac{3a_3a_5 + 2a_2a_4}{c\delta_1} + [2a_4^2 + 3a_5^2 + (a_3 + \chi_1 a_5)^2]\frac{\beta_1 + \beta_2}{\beta_1 - \beta_2} \\ &\quad - [2a_4^2 + 3A_5^2 + (a_3 + \chi_1 a_5)(a_3 + \chi_2 a_5)]\frac{2\beta_2}{\beta_1 - \beta_2}\frac{\delta_2}{\delta_1} \\ A_{12} &= 2a_2a_3 + 4a_2a_5\chi_1 + 5a_3a_4\chi_1 + 9a_4a_5\chi_1^2 + \frac{2a_2a_5}{c\delta_1} \\ &\quad + [2a_4a_5 + a_4(a_3 + \chi_1 a_5)]\frac{\beta_1 + \beta_2}{\beta_1 - \beta_2} - [2a_4a_5 + a_4(a_3 + \chi_2 a_5)]\frac{2\beta_2}{\beta_1 - \beta_2}\frac{\delta_2}{\delta_1} \\ A_{13} &= a_3^2 + 2a_2a_4 + 5a_3a_5\chi_1 + 3a_4^2\chi_1 + 5a_5^2\chi_{1\&2} + a_5(a_3 + \chi_1 a_5)\frac{\beta_1 + \beta_2}{\beta_1 - \beta_2} \\ &\quad - a_5(a_3 + \chi_2 a_5)\frac{2\beta_2}{\beta_1 - \beta_2}\frac{\delta_2}{\delta_1} \\ A_{14} &= 2a_2a_5 + 2a_3a_4 + 6a_4a_5\chi_1 \\ A_{15} &= 2a_3a_5 + a_4^2 + 3a_5^2\chi_1 \\ A_{16} &= 2a_4a_5 \\ A_{17} &= a_5^2 \end{aligned} \quad \text{(B.19)}$$

Appendix B

$$A_{21} = A_{11} - 2[2a_4^2 + 3a_5^2 + (a_3 + \chi_1 a_5)(a_3 + \chi_2 a_5)]\frac{\delta_2}{\delta_1} - \frac{3a_3a_5 + 2a_4a_2}{c\delta_1}(1 + c)$$

$$A_{22} = A_{12} - 2[2a_4a_5 + a_4(a_3 + \chi_2 a_5)]\frac{\delta_2}{\delta_1} - \frac{2a_2a_5}{c\delta_1}(1 + c)$$

$$A_{23} = A_{13} - 2a_5(a_3 + \chi_2 a_5)\frac{\delta_2}{\delta_1}$$

$$A_{2k} = A_{1k} \qquad (k = 4,\ldots,7) \tag{B.20}$$

The coefficients p_1, B_{1k}, B_{2k} are found from the expressions for M_1, A_{1k}, A_{2k} by substitution of β_1, β_2, δ_1, δ_2, κ_1, κ_2 by β_2, β_1, δ_2, δ_1, κ_2, κ_1 respectively.*

Reference

1. Savin G.N., *Stress Distribution around Holes*, NASA Technical Translation F-607, November 1970.

Author: Eichenberger Edward Peter.
Name of thesis: A photoelastic investigation into the stress concentration factors around rectangular holes in composite plates.

PUBLISHER:
University of the Witwatersrand, Johannesburg
©2015

LEGALNOTICES:

Copyright Notice: All materials on the University of the Witwatersrand, Johannesburg Library website are protected by South African copyright law and may not be distributed, transmitted, displayed or otherwise published in any format, without the prior written permission of the copyright owner.

Disclaimer and Terms of Use: Provided that you maintain all copyright and other notices contained therein, you may download material (one machine readable copy and one print copy per page)for your personal and/or educational non-commercial use only.

The University of the Witwatersrand, Johannesburg, is not responsible for any errors or omissions and excludes any and all liability for any errors in or omissions from the information on the Library website.